

ABSTRACT

SUPERCONDUCTING PROPERTIES OF $\text{ZrNi}_{2-x}\text{TM}_x\text{Ga}$ (TM = Cu, Co) AND $\text{ZrNi}_2\text{Al}_x\text{Ga}_{1-x}$ HEUSLER COMPOUNDS

by Dharma Raj Basaula

The superconducting properties of a series of $\text{ZrNi}_{2-x}\text{TM}_x\text{Ga}$ (TM = Cu, Co) and $\text{ZrNi}_2\text{Al}_x\text{Ga}_{1-x}$ Heusler compounds have been explored by x-ray diffraction, scanning electron microscopy, electrical resistivity, dc magnetization and ac susceptibility measurements. In common, all samples exhibited the cubic $L2_1$ Heusler structure at room temperature. For $x \leq 0.25$, the $\text{ZrNi}_{2-x}\text{Cu}_x\text{Ga}$ compounds demonstrated superconductivity and the superconducting transition temperature, T_c , decreased with increasing Cu concentration. The dc magnetization data suggested the type-II superconductivity for all the Cu-doped compounds. Unlike $\text{ZrNi}_{2-x}\text{Cu}_x\text{Ga}$, up to the lowest measuring temperature of 1.75 K, no superconductivity was observed in any of the $\text{ZrNi}_{2-x}\text{Co}_x\text{Ga}$ compounds. All the Al-doped compounds also showed type-II superconductivity with a decrease in T_c . In addition, the $\text{ZrNi}_2\text{Al}_x\text{Ga}_{1-x}$ compounds showed a new phase transition a few kelvins above superconducting transition. The experimental results are presented and discussed in detail.

SUPERCONDUCTING PROPERTIES OF $\text{ZrNi}_{2-x}\text{TM}_x\text{Ga}$ (TM = Cu, Co) AND $\text{ZrNi}_2\text{Al}_x\text{Ga}_{1-x}$
HEUSLER COMPOUNDS

Thesis

Submitted to the
Faculty of Miami University
in partial fulfillment of
the requirements for the degree of
Master of Science

by

Dharma Raj Basaula

Miami University

Oxford, Ohio

2018

Advisor: Dr. Mahmud Khan

Reader: Dr. Herbert Jaeger

Reader: Dr. Khalid Eid

©2018 Dharma Raj Basaula

This thesis titled

SUPERCONDUCTING PROPERTIES OF $\text{ZrNi}_{2-x}\text{TM}_x\text{Ga}$ (TM = Cu, Co) AND $\text{ZrNi}_2\text{Al}_x\text{Ga}_{1-x}$
HEUSLER COMPOUNDS

by

Dharma Raj Basaula

has been approved for publication by

The College of Arts and Science

and

Department of Physics

Dr. Mahmud Khan

Dr. Herbert Jaeger

Dr. Khalid Eid

Table of Contents

Chapter 1: Introduction.....	1
Chapter 2: Background and Theory.....	4
2.1 Historical background	4
2.2 Theoretical Models.....	7
2.2.1 London Equations	7
2.2.2 Ginzburg-Landau Theory.....	9
2.2.3 BCS Theory	11
2.3 Type I and Type II Superconductors.....	14
2.4 High Temperature Superconductors.....	17
2.5 Heusler Superconductors.....	18
Chapter 3: Experimental Methods	22
3.1 Sample Preparation	22
3.2 Structural Characterization and Analysis.....	23
3.2.1 X-ray Diffraction Theory	23
3.2.2 X-ray Diffractometer	24
3.2.3 X-ray Diffraction Analysis	26
3.3 Compositional Characterization and Analysis	27
3.3.1 Scanning Electron Microscopy: Theory	27
3.3.2 Energy-Dispersive X-ray Spectroscopy.....	28
3.4 Resistivity and Magnetization Measurement	29
3.4.1 The Physical Property Measurement System	30
3.4.2 Vibrating Sample Magnetometer (VSM).....	35
3.4.3 AC Magnetometer.....	37
Chapter 4: Results and Discussion	38
4.1 Structural properties	39

4.1.1 X-ray diffraction	39
4.1.2 Scanning Electron Microscope	43
4.2 Resistivity Measurements:	47
4.2.1 Temperature dependent Resistivity, $R(T)$	47
4.2.2 Resistivity versus Magnetic field, $\rho(H)$	50
4.3 Magnetization measurements.....	50
4.3.1 Magnetization versus Temperature, $M(T)$	51
4.3.2 Magnetization versus Magnetic Field, $M(H)$	55
4.3.3 AC Susceptibility versus temperature.....	59
Chapter 5: Conclusion	61
References.....	63

List of Tables

Table 1 Some Heusler compounds with their Tc.....	19
Table 2 A list of $\text{ZrNi}_{2-x}\text{TM}_x\text{Ga}$ samples.	38
Table 3 A list of $\text{ZrNi}_2\text{Ga}_{1-x}\text{Al}_x$ samples.....	38

List of Figures

Figure 2.1 Resistance (ohm) versus Temperature (K) [1]	5
Figure 2.2 A graphical explanation of Meissner Effect [23]	6
Figure 2.3 Type I (a) and Type II (b) superconductors with length scales, λ and ξ , in accordance with Landau parameter. [39].....	11
Figure 2.4 Formation of Cooper pair according to BCS theory [40].....	12
Figure 2.5 Temperature dependence of energy gap in BCS theory [41]	13
Figure 2.6 Behavior of electronic specific heat near and below T_c [41].....	14
Figure 2.7 Magnetic behavior of a Type I superconductor. [43]	15
Figure 2.8 Magnetic behavior of a Type II superconductor [43].....	16
Figure 2.9 Formation of tubes in different phases of a superconductor [46].....	17
Figure 2.10 Elements forming Heusler alloys [52].....	19
Figure 2.11 $L2_1$ cubic structure of a Heusler alloy [59]	20
Figure 2.12 Electronic band structure (a) and the density of states (b) of $ZrNi_2Ga$ with Van Hove singularity in inset of (b) [11]	21
Figure 3.1 Schematic representation of Bragg's law [63]	24
Figure 3.2 Scintag x-ray diffractometer.....	25
Figure 3.3 Components of an x-ray Diffractometer [64].....	26
Figure 3.4 Components of Scanning Electron Microscope (SEM) [66].....	27
Figure 3.5 EDS spectrum showing various transitions [67]	29
Figure 3.6 Resistivity puck [68].....	30
Figure 3.7 Block Diagram of PPMS [68]	32
Figure 3.8 Components of the PPMS Probe [68]	34
Figure 3.9 Components of VSM-PPMS system [68].....	36

Figure 3.10 ACMS parts and cross-sectional view of coil [68].....	37
Figure 4.1 X-ray diffraction pattern of $ZrNi_{2-x}Cu_xGa$ and $ZrNi_{2-x}Co_xGa$ compounds	40
Figure 4.2 X-Ray diffraction pattern of $ZrNi_2Ga_{1-x}Al_x$ compounds	41
Figure 4.3 Variation of lattice parameter in Cu and Co-doped compounds	42
Figure 4.4 Variation of Lattice parameter in Al-doped compounds.....	42
Figure 4.5 SEM images of Cu-doped compounds	43
Figure 4.6 SEM images of Co-doped samples.....	44
Figure 4.7 SEM micrographs of the Cu doped compounds with $x = 0.25$. (left) and Co doped sample (right) with $x = 0.25$	45
Figure 4.8 SEM images of Al-doped samples	46
Figure 4.9 Temperature dependence of the resistivity for $ZrNi_{2-x}Cu_xGa$	47
Figure 4.10 Temperature dependence of the resistivity for $ZrNi_{2-x}Co_xGa$	48
Figure 4.11 Temperature dependent resistivity of $ZrNi_2Ga_{1-x}Al_x$	49
Figure 4.12 Normalized resistivity versus magnetic field for $ZrNi_{2-x}Cu_xGa$	50
Figure 4.13 The dc magnetization of $ZrNi_{2-x}Cu_xGa$. The inset shows T_C as a function of Cu concentration x	52
Figure 4.14 The dc magnetization of $ZrNi_2Ga_{1-x}Al_x$ compounds.....	53
Figure 4.15 The dc magnetization of $ZrNi_2Al_{0.25}Ga_{0.75}$	54
Figure 4.16 Field dependence of the magnetization of $ZrNi_{2-x}Cu_xGa$ measured at 2 K.....	56
Figure 4.17 Field dependence of the magnetization of $ZrNi_{2-x}Co_xGa$ measured at 2 K.....	57
Figure 4.18 Field dependence of the magnetization of $ZrNi_2Ga_{1-x}Al_x$ measured at 2 K.	58
Figure 4.19 Real components of the ac susceptibility of selected $ZrNi_{2-x}Cu_xGa$ compounds.....	59
Figure 4.20 Real components of the ac susceptibility of selected $ZrNi_2Ga_{1-x}Al_x$ compounds.	60

Dedication

To my family and friends

Acknowledgements

I am heartily grateful to my advisor Dr. Mahmud Khan for his relentless support in and outside the lab to prepare this thesis project. I would like to thank Dr. Herbert Jaeger and Dr. Khalid Eid for being my committee members. My labmates Saad Alzaahrani, Jeffrey Brock and Zeeshan Ali are equally appreciated for their support.

Chapter 1: Introduction

Intermetallic alloys exhibit many extraordinary properties like high thermal resistance, high melting point and high resistance against electrochemical corrosion. Due to their strong crystallinity and mixed bonding they also exhibit interesting magnetic and other physical properties. Because of these special properties, intermetallic compounds have a wide range of application in automotive and aerospace industries, electronics, robotics, magnetic storage, and many other technologies.

Superconductivity, which was discovered by H K Onnes in 1911,¹ is one of many interesting properties of selected intermetallic alloys. The fundamental properties of a superconductor, which can be highlighted in the zero resistivity below the superconducting transition temperature, T_C , and its ability of expelling the magnetic field from its interior have always fascinated the scientists and have brought new applications into existence.

The first discovery of superconductivity was in elemental Mercury, which at that time could be refined to a highly pure form. It exhibited a T_C of 4.2 K above which it showed roughly linear temperature dependence of resistivity and below which it showed virtually zero resistivity.¹ Years later, in 1934, the first superconducting compound, $PbTl_2$, was discovered that exhibited a T_C of 3.8 K.² Since then, superconductivity has been discovered in many materials and several applications have been derived from them. Among the most remarkable applications are the Nb_3Sn and $NbTi$ based superconducting magnets, and infrared light detectors based on NbN .³ In 1987, superconductivity was discovered in $YBa_2Cu_3O_7$, a cuprate-perovskite ceramic material, with a T_C of 93 K, well above the boiling point of liquid nitrogen, which is ~ 77 K.⁴ In 2015, a T_C of 203 K was achieved in H_2S gas under high pressure.⁵ These significant advancements indicate a promising future of room temperature superconductors.

Several theories have been proposed to explain superconductivity at microscopic level. The BCS theory developed by Bardeen, Cooper, and Schrieffer in 1957 is the most convincing one until now.⁶ According to this theory, below T_C , electrons interact with crystal lattice via phonon interaction to form electron pairs called Cooper pairs, which are termed as the superconducting

charge carriers. The Cooper pair exhibit Boson-like nature by condensing in energy levels near Fermi level, and since their energy is extremely weak, they can be destroyed by a small increase in temperature. Additionally, an energy gap is created above the condensed Cooper pairs since their energy is very low. This energy gap is represented by the transition temperature T_C above which, the material behaves normally and becomes superconducting below it. The BCS theory is perfect for describing the conventional superconductors with very low T_C , but the theory cannot be applied to all superconductors.

Superconductors exhibit an interesting phenomenon called Meissner effect in which an external magnetic field is repelled from inside the superconductor until the field becomes large enough to destroy the superconductivity.⁷ Based on this property, superconductors are divided into two types.⁸ In type-I superconductors, superconductivity is destroyed above a critical magnetic field, H_C , and most of them are pure elements.⁹ In type-II superconductors, there are two critical fields. At the lower critical field, H_{C1} , the magnetic vortices start to develop and penetrate the superconductor while the superconductivity persists, and when raising the applied magnetic field to be above the higher critical field, H_{C2} , the superconductivity is completely destroyed.

In 1982, Heusler alloys with an ideal formula of AB_2C with a rare-earth metal in the B position, were reported to be superconducting.¹⁰ That discovery motivated researchers to look for non-rare-earth based Heusler superconductors with the same formula of AB_2C . $ZrNi_2Ga$ is a Ni based Heusler alloy with a superconducting T_C of 2.87 K.¹¹ Nearly 19 Heusler alloy based superconductors have been discovered with 27 valence electrons per formula unit with an average of 6.75 electrons per atom.¹² In these materials, superconductivity has been explained in terms of the van Hove singularities, which refers to a saddle point in the energy dispersion curves of the electronic structure of the respective material.¹³ $ZrNi_2Ga$ was shown to be a weakly coupled BCS type-II superconductor, with a paramagnetic state above T_C . It was also shown that partial replacement of Zr by Nb broadened the van Hove singularity while creating a higher degree of disorder in $Zr_{1-x}Nb_xNi_2Ga$, causing T_C to decrease across the system. The partial replacement of Ni by Zr or of Zr by Ni in $Zr_{1+x}Ni_{2-x}Ga$ and $Zr_{1-x}Ni_{2+x}Ga$ compounds, respectively, dramatically diminished the SC properties and enhanced the paramagnetic interactions in the doped materials.¹⁴

The effect of elemental doping on the superconducting properties of $\text{ZrNi}_{2-x}\text{TM}_x\text{Ga}$ ($\text{TM} = \text{Cu}, \text{Co}$) and $\text{ZrNi}_2\text{Ga}_{1-x}\text{Z}_x$ ($\text{Z} =$ main group elements) have not been studied to-date. While Cu is a non-ferromagnetic material and has one more electron than Ni, Co is ferromagnetic and has one less electron. Therefore, it is of fundamental interest to explore the superconducting properties of $\text{ZrNi}_{2-x}\text{TM}_x\text{Ga}$. Additionally, the effect of Z element doping on the superconducting properties of $\text{ZrNi}_2\text{Ga}_{1-x}\text{Z}_x$ system is also of fundamental interest. Therefore, in the proposed thesis project, the structural, magnetic and transport properties of the $\text{ZrNi}_{2-x}\text{TM}_x\text{Ga}$ and $\text{ZrNi}_2\text{Ga}_{1-x}\text{Al}_x$ systems have been investigated in detail.

Chapter 2: Background and Theory

2.1 Historical background

In 1908, the great Dutch Physicist H.K. Onnes cherished one of the most exciting moment of his career in his laboratory at Leiden University. He had first liquefied helium at extremely low temperature and that led to a whole new chapter in the field of low-temperature physics. After the discovery, it was obvious for him to start conducting experiments of various properties of different materials at that temperature regime. At that time, it was of great interest in the world of physics regarding the resistivity of metals as the temperature approached absolute zero. Onnes then stepped up to measure the resistivity of various pure metals and the striking result came out for mercury, the resistivity of which dropped sharply to zero at 4.2 K in the near periphery of boiling point of helium. To convince himself, he repeated the experiment several times to confirm the zero resistivity before he reported the results. He quoted this extremely new phenomenon as “practical zero” or superconductivity. Figure 2.1 shows the first ever recorded resistance versus temperature data of mercury showing zero resistivity.

After the discovery of superconductivity in mercury, lots of other pure metals were tested for their resistivity below the boiling point of liquid helium. Some of the early superconducting metals are lead (Pb) ($T_c=7.2\text{K}$)¹⁵, Niobium (Nb, $T_c=9.2\text{K}$)¹⁶, Vanadium (V, $T_c=5.3\text{K}$)¹⁷, Lanthanum (La, $T_c=4.8\text{K}$)¹⁸, Tin (Sn, $T_c=3.7\text{K}$)¹⁹, Aluminum (Al, $T_c=1.18\text{K}$)²⁰, Indium (In, $T_c=3.4\text{K}$)²¹, Zinc (Zn, $T_c=0.85\text{K}$)²¹.

Until 1923, only Onnes’ laboratory had the helium liquefaction facility and the low temperature-based experiments were limited in that lab only. Later on, the procedure was adopted by other famous labs and the research went on progressively. In 1933, a key experimental milestone was achieved when German scientists Walther Meissner and Robert Ochsenfeld found an exciting new magnetic behavior of tin at its superconducting state²¹. They observed that a tin cylinder cooled to its superconducting state under a constant magnetic field would deflect the orientation of the compass needles. This is possible only if the tin itself produces a magnetic field from its interior and that was what exactly was happening. This field effect is known as the Meissner effect.

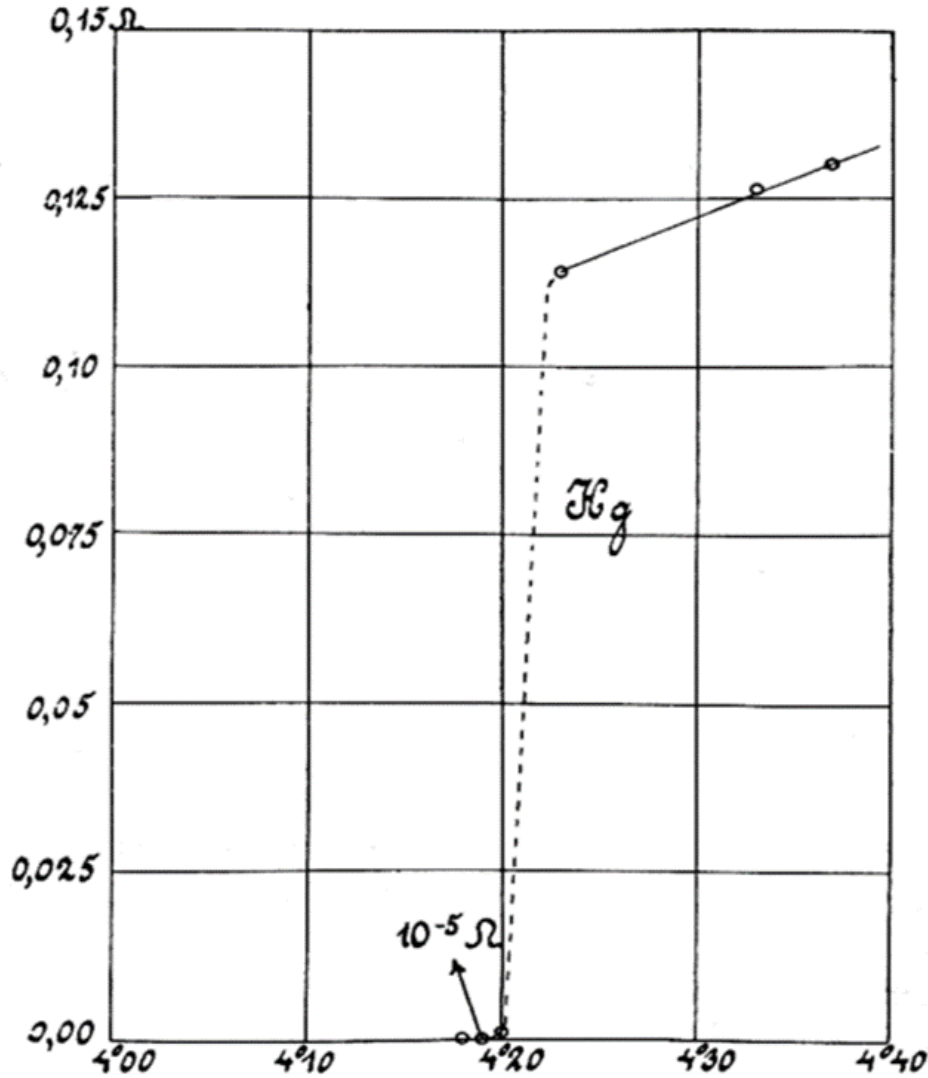


Figure 2.1 Resistance (ohm) versus Temperature (K) [1]

After the discovery of Meissner effect, Fritz and Heinz London came up with a phenomenological explanation of electromagnetic theory of superconductivity for the first time where they predicted the minimization of electromagnetic free energy in the superconducting state²². In 1935, it was shown that the single crystal of PbTi_2 exhibited two distinct critical fields, H_{c1} and H_{c2} , unlike that of previously discovered superconductors²⁵. The flux is excluded up to a lower critical field H_{c1} and it starts penetrating the superconductor until an upper critical field H_{c2} is reached and the superconductivity is completely lost. This class of superconductors showing two critical fields

were then termed as type II superconductors. Most of the alloys and compound superconductors fall in this class.

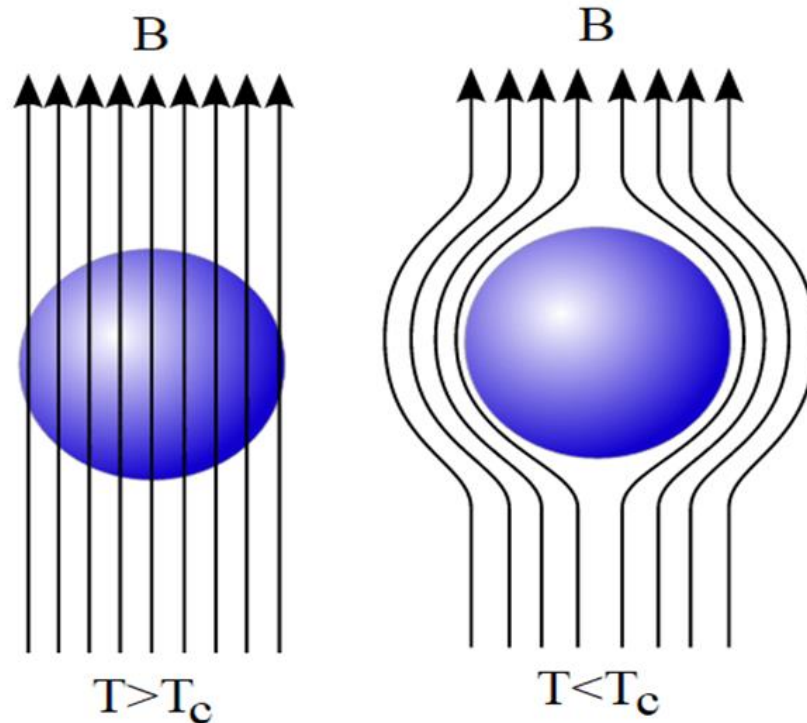


Figure 2.2 A graphical explanation of Meissner Effect [23]

The hunt for superconductivity was not only limited to pure metals. Several alloys were discovered that exhibited a superconducting critical temperature larger than that of pure metals^{24, 25, 26}. The discovery of Nb_3Sn whose transition temperature was 18.3 K with high critical magnetic field, led to the applications of superconductors²⁷. In 1962, another extremely useful superconducting alloy, NbTi was discovered, which is used in several applications as of now making it the most commercialized superconductor²⁸.

The research in superconductivity was impeded until the decade of 1980s where some significant discoveries were made. In the year 1982, the first two Heusler superconductors were discovered namely YPd_2Sn and YPd_2In . In the year 1986, there was an important breakthrough in high temperature superconductivity where researchers were able to find several ceramic superconductors with superconducting critical temperature, T_c , well above the boiling point of liquid nitrogen^{29, 30, 31}. The quest for high temperature superconductors has progressed a lot in

recent years following the discoveries of cuprates and iron pnictides^{32, 33}. A most recent remarkable discovery with highest T_c of 203 K has been made for H₂S under a very high pressure of 150 GPa³⁴ followed by the discovery of metallic H₂S under an applied pressure of 100 GPa³⁵.

2.2 Theoretical Models

The experimental observation of superconductivity led to the development of many theoretical models that tried to explain this fascinating phenomenon. These models are based on quantum mechanical, thermodynamical, and microscopical terms. A brief discussion on the most commonly known theories is presented below.

2.2.1 London Equations

After the discovery of Meissner effect in superconductors in 1933, two brothers Fritz and Heinz London came up with a phenomenological theory, which could explain superconductivity to some extent²³. They proposed a set of two equations compatible with Maxwell's equations and electromagnetism, but they couldn't explain the thermodynamics and quantum phenomena behind it. The first London equation is based on the idea that the resistivity of a material is due to the movement of electrons within the material by means of phonon scattering and other electromagnetic interactions. The London equations incorporate the electromagnetic fields and current within the superconductor. They proposed that, in a superconductor, the Ohm's law should be replaced by a changing current density that can be related to the electric field by the following equation;

$$\frac{\partial \mathbf{J}}{\partial t} = \frac{n_s e^2}{m} \mathbf{E} \quad \text{Equation 1}$$

Where J is the superconducting current density, E is the electric field within the superconductor, e is the electronic charge, m is the mass of an electron, and n_s is the phenomenological constant associated with superfluid density³⁶. In the above equation, if the electric field within the superconductor is zero, it will lead to a persistent current inside the superconductor creating a constant magnetic field. Later, however, the London brothers found that the solution of this

equation was not compatible with the Meissner effect. But they soon realized that they could get rid of the time derivatives in current density and magnetic field by taking the curl of above equation which will give the second London equation as:

$$\nabla \times \mathbf{J} = -\frac{n_s e^2}{m} \mathbf{B} \quad \text{Equation 2}$$

Where \mathbf{B} is the magnetic field within the superconductor.

These two equations can be represented by a single equation introducing a vector potential \mathbf{A} as follows

$$\mathbf{J} = -\frac{n_s e^2}{m} \mathbf{A} \quad \text{Equation 3}$$

Where the divergence of the vector potential is zero in the Coulomb Gauge condition in which the vector potential \mathbf{A} tends to vanish inside the superconductor and the normal component over the surface can be related through the above equation³⁷.

If we take curl of the second London equation and substitute Ampere's law, we come up with the following differential equation

$$\nabla^2 \mathbf{B} = \frac{1}{\lambda^2} \mathbf{B} \quad \text{Equation 4}$$

Where, $\lambda = \sqrt{\frac{m}{\mu_0 n_s e^2}}$ is a characteristic length scale known as "London penetration depth" to which the magnetic field can penetrate through the superconductor. If we imagine a magnetic field of magnitude \mathbf{B}_0 parallel to the boundary plane in z-direction and penetrating through a superconductor along x-axis, then the solution to the above equation gives the varying magnetic field as,

$$\mathbf{B}_z(x) = \mathbf{B}_0 e^{-x/\lambda} \quad \text{Equation 5}$$

This shows that the magnitude of penetrating field decreases exponentially inside the superconductor.

2.2.2 Ginzburg-Landau Theory

Vitaly Lazarevich Ginzburg and Lev Landau introduced a mathematical physical theory based on thermodynamical perspectives³⁸. Landau, who is famously known for his work on thermodynamic phase transitions, and Ginzburg proposed that the Gibb's free energy of a superconductor in the vicinity of superconducting transition can be defined by introducing a complex order parameter, ψ , which is a microscopic ground state wave function. Below the superconducting transition, this complex parameter has a non-vanishing value that depends on the density of superconducting components. The Gibb's free energy, F , in terms of ψ can be expressed as follows:

$$F = F_n + \alpha|\psi|^2 + \frac{\beta}{2}|\psi|^4 + \frac{1}{2m}|(-i\hbar\nabla - 2e\mathbf{A})\psi|^2 + \frac{|\mathbf{B}|^2}{2\mu_0} \quad \text{Equation 6}$$

Where F_n is the Gibb's free energy above the superconducting transition, α and β are the phenomenological constants, e and m are the charge and effective mass of an electron, \mathbf{B} is the magnetic field expressed in terms of magnetic vector potential \mathbf{A} . The Gibb's free energy equation can be minimized in terms of the order parameter ψ to obtain the following equations,

$$\alpha\psi + \beta|\psi|^2\psi + \frac{1}{2m}(-i\hbar\nabla - 2e\mathbf{A})^2\psi = 0 \quad \text{Equation 7}$$

This equation determines the order parameter. And the current density is given by,

$$\mathbf{J} = \frac{2e}{m} \text{Re}\{\psi * (-i\hbar\nabla - 2e\mathbf{A})\psi\} \quad \text{Equation 8}$$

which gives the superconducting current.

The first Ginzberg-Landau equation can be solved in 1D to find a measurable quantity called coherence length in the vicinity of superconducting state transition. The solution in 1D to the first equation near the transition is given by,

$$\psi(x) = |\psi|e^{-x/\xi} \quad \text{Equation 9}$$

$$\text{Where, } \xi = \sqrt{\frac{\hbar^2}{2m|\alpha|}} \quad \text{Equation 10}$$

For $T > T_c$

And,

$$\xi = \sqrt{\frac{\hbar^2}{4m|\alpha|}} \quad \text{Equation 11}$$

For $T < T_c$

This coherence length ξ is a measure of how fast the wave function can vary in space. If the coherence length is small, the macroscopic wave function of superconducting charges can be changed in an abrupt manner. The larger coherence length means that the wave function has a higher rigidity and it can vary in a gradual manner over the space. The coherence length diverges near T_c .

The London penetration depth, λ , can be modified in terms of Ginzberg-Landau parameters as

$$\lambda = \sqrt{\frac{m}{4\mu_0 e^2 \psi_0^2}} \quad \text{Equation 12}$$

Where ψ_0 represents the order parameter in absence of electromagnetic field. These two characteristic length scales, λ and ξ , can be correlated to define a new parameter κ , which is the ratio of the penetration depth to the Ginzberg-Landau parameter. This ratio κ has a significant importance in the transition region. As proposed by Landau, the ratio $\kappa = \lambda/\xi$ is less than $\frac{1}{\sqrt{2}}$ for a Type I superconductor and is greater than $\frac{1}{\sqrt{2}}$ for a Type II superconductor, which can be depicted graphically as in Figure 2.3.

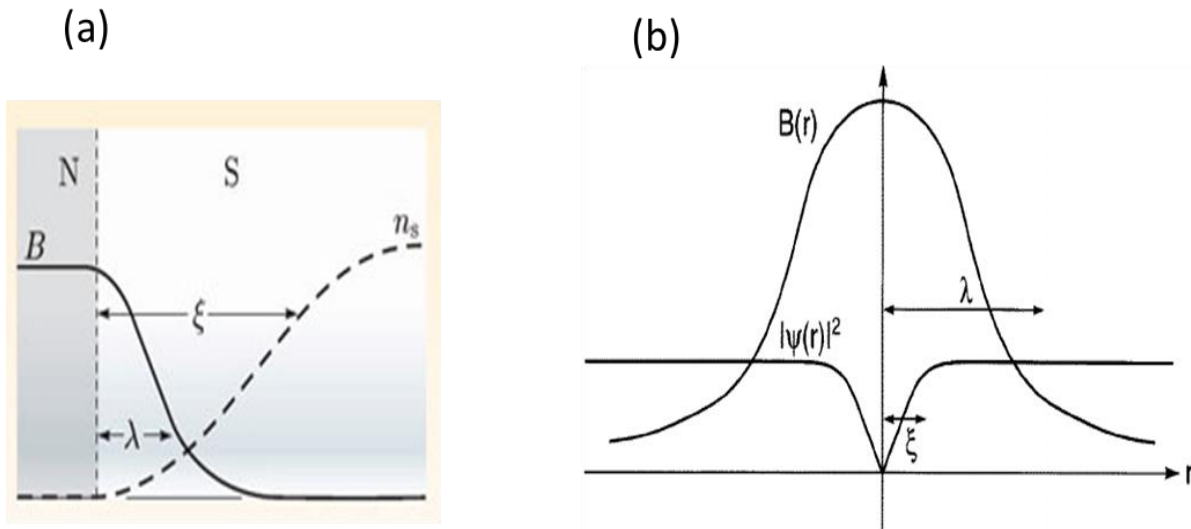


Figure 2.3 Type I (a) and Type II (b) superconductors with length scales, λ and ξ , in accordance with Landau parameter. [39]

2.2.3 BCS Theory

The first microscopic theory describing superconductivity came in 1957 as the BCS theory of superconductivity proposed by John Bardeen, Leon Cooper and Robert Schrieffer.⁶ The BCS theory is based on the assumption that, at very low temperature, the normal state Fermi surface collapses into a coherent many-body condensate of bound electron pairs known as Cooper pairs. The formation of the Cooper pair is mainly based on the idea that the Coulomb repulsion between the paired electrons tends to be screened out by the positively charged ions and electron clouds. The attractive interaction between electrons comes from the interaction between freely moving electrons and the lattice phonons.

According to this theory, the positively charged ions in lattice attract a freely moving electron causing a distortion in the lattice. This distortion creates a region of higher positive charge density which attracts another electron but with opposite momentum. These two electrons with opposite spins are now correlated and move together throughout the lattice. In the superconducting state, these electron pairs form a condensate of bosons having same energy state near the Fermi level. If a pair in this condensate state breaks, then the entire system loses the bound energy associated with the pairing and the state is no more superconducting. The oscillating energy from atoms in the

lattice at low temperature is not sufficient to break this pairing energy barrier. As such, the whole condensate of the electron pairs moves with no resistance within the conductor. The formation of electron pair can be depicted as in Figure 2.4

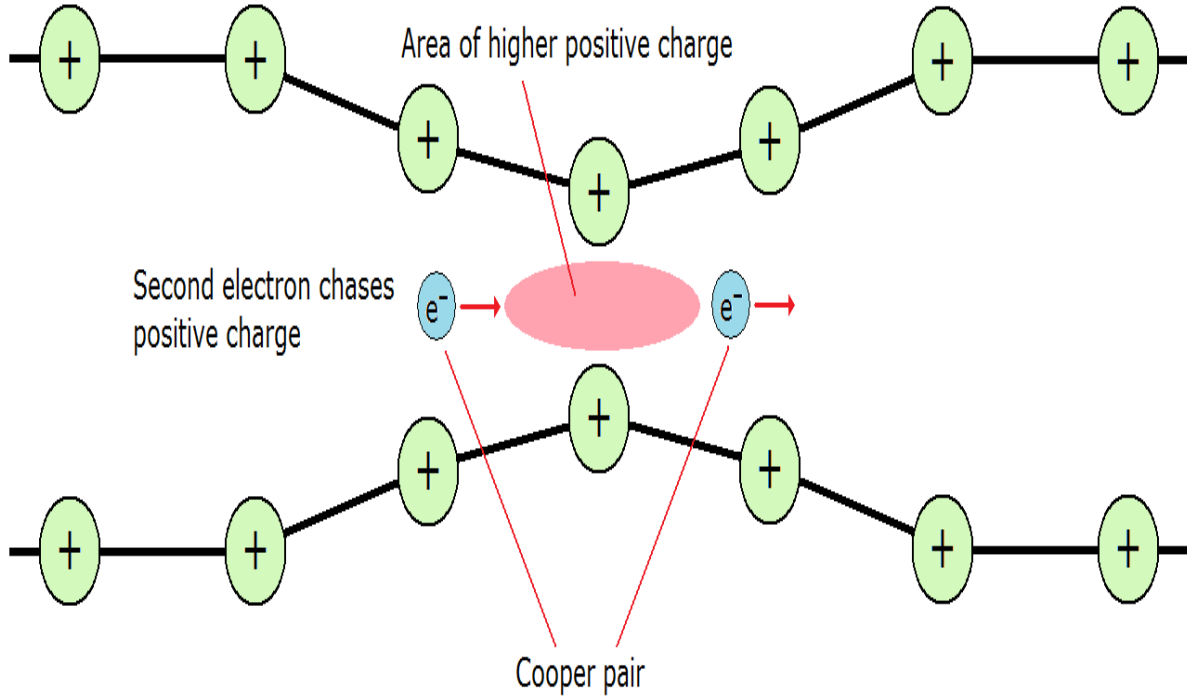


Figure 2.4 Formation of Cooper pair according to BCS theory [40]

The quantitative description of The BCS theory is based on the value of energy gap of Cooper pairs. The electrons are correlated in Cooper pairs due to the Pauli Exclusion Principle and form an energy gap between single electron levels and Cooper pair levels. This energy gap is such that the breaking of a single pair of electron requires the change in energy of all other remaining pairs. This gap grows with the increase in attractive interaction between the paired electrons and the single particle density of states near Fermi level. The dependence of this energy gap at any temperature T on the superconducting critical temperature T_c can be related by the following universal ratio,

$$\frac{\Delta(T = 0)}{T_c} = 1.764\kappa_B \quad \text{Equation 13}$$

Where, κ_B is the Boltzmann constant. This relation holds for any material in weak coupling case. The energy gap drops to zero near T_c as

$$\frac{\Delta(T)}{\Delta(0)} \approx 1.74 \left(1 - \frac{T}{T_c}\right)^{1/2} \quad \text{Equation 14}$$

The following graph shows the temperature dependence of energy gap in a superconductor⁴¹.

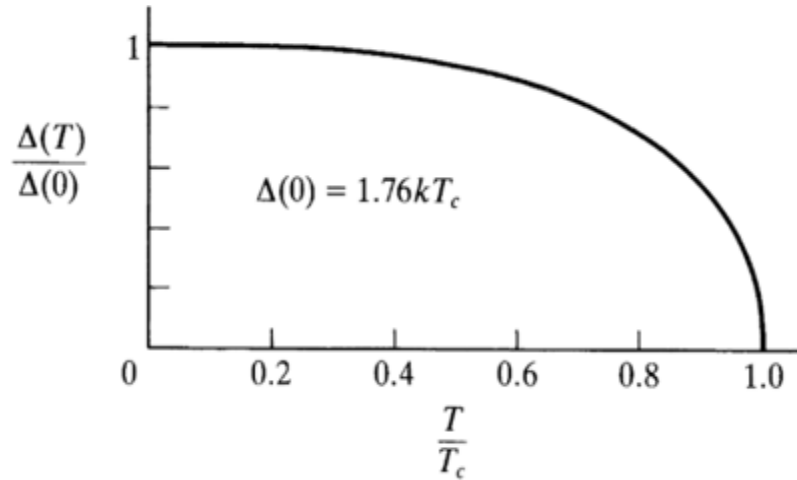


Figure 2.5 Temperature dependence of energy gap in BCS theory [41]

This energy gap is also responsible for the exponential suppression of heat capacity of superconductors at low temperatures. But just before the transition temperature, there is a discontinuity in electronic specific heat showing a sudden jump at T_c . The temperature dependence of electronic heat capacity in this transition region can be expressed mathematically as

$$\frac{C}{\gamma T_c} = 1.34 \left(\frac{\Delta(0)}{\kappa_B T}\right)^{3/2} e^{-\Delta(0)/\kappa_B T} \quad \text{Equation 15}$$

The behavior of electronic specific heat at T_c can be illustrated graphically as in Figure 2.6.

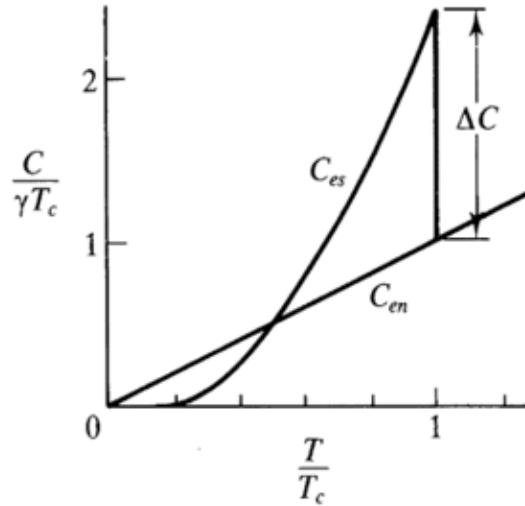


Figure 2.6 Behavior of electronic specific heat near and below T_c [41]

Although the BCS theory explains the low temperature superconductivity correctly, it's assumption that the highest superconducting transition temperature should not exceed 30 K fails to explain the high temperature superconductivity that were discovered in cuprate perovskites and iron pnictides which exceed the boiling point of liquid nitrogen⁴². So, there is still an unknown mechanism that needs to be discovered to explain high temperature superconductivity.

2.3 Type I and Type II Superconductors

On the basis of response to applied magnetic field, superconductors can be divided into two types. Type I superconductors are recognized by the occurrence of first order phase transition where the superconductivity is completely destroyed beyond a critical magnetic field H_c . Mostly, pure metals and a few alloys show this type of transition^{43,44}. The magnetic behavior of type I superconductors is as shown in Figure 2.7⁴⁵.

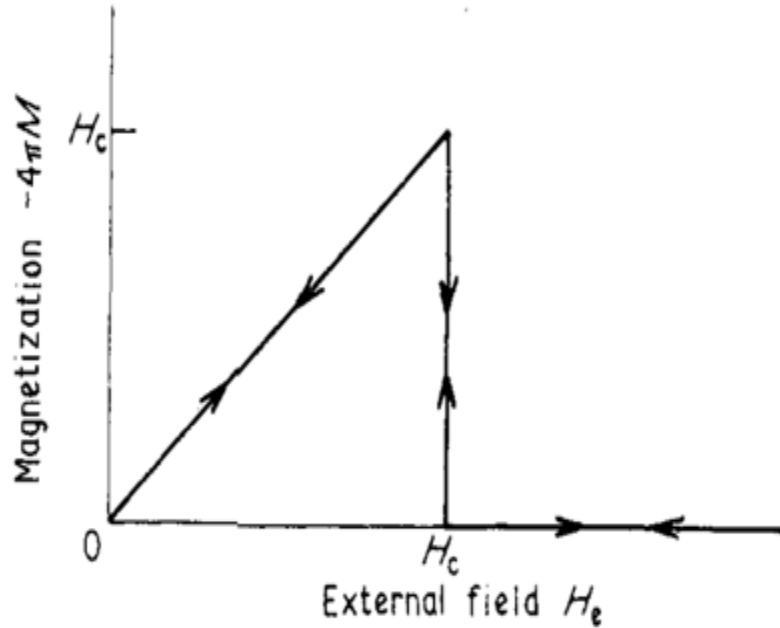


Figure 2.7 Magnetic behavior of a Type I superconductor. [43]

Below the critical field, the superconductor behaves as an ideal diamagnet exactly offsetting the applied field.

The 2nd type is a Type II superconductor that is characterized by two critical magnetic fields. The superconductivity in this class of materials does not destroy abruptly rather it decreases gradually from a lower critical field H_{c1} to an upper critical field H_{c2} beyond which it is completely destroyed. In contrast to Type I superconductor, Type II superconductor shows magnetic behavior as shown in Figure 2.8. Unlike the type I superconductors, type II superconductors show the diamagnetic behavior until the lower critical field H_{c1} is reached and above this field, the magnetization gradually falls off expelling magnetic field partially. However, the resistivity remains zero throughout the mixed state and returns to normal phase only above the upper critical field.

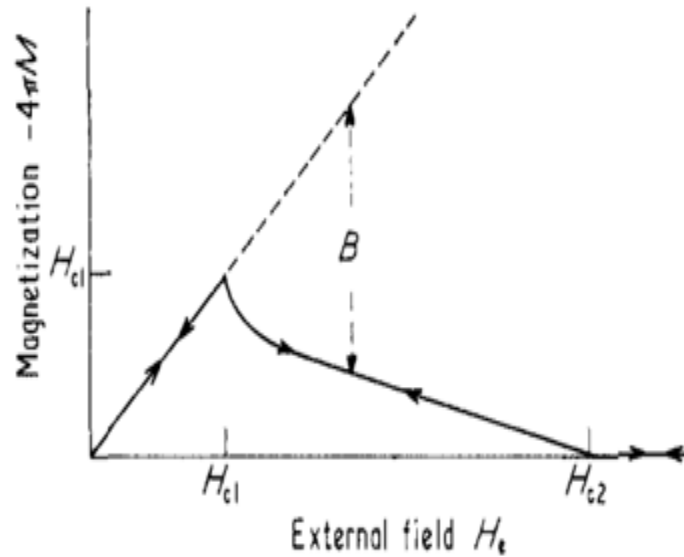


Figure 2.8 Magnetic behavior of a Type II superconductor [43]

Between the upper and lower critical field is the mixed state of Meissner effect and flux pinning. The magnetic flux lines are not completely expelled, and they can penetrate through the superconductor. The field lines penetrate through the superconductor in the form of vortices. Just above the lower critical field H_{c1} , the Gibb's free energy associated with the vortices is greater than that in the Meissner state and the flux is able to penetrate through the superconductor. In this vortex state, small tubes of counter circulating current are formed which increase in number going from lower to upper critical field. These tubes, as shown in Figure 2.9, are quantized and pass only a single quantum of magnetic flux known as fluxon.

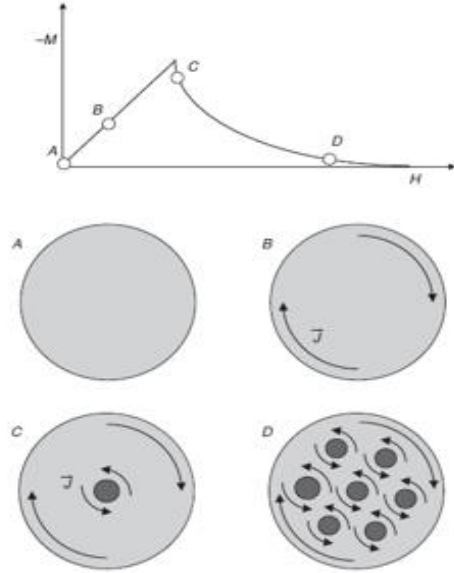


Figure 2.9 Formation of tubes in different phases of a superconductor [46]

The lower critical field from where the vortex starts to form can be expressed in terms of penetration depth as,

$$H_{c1} = \frac{\phi_0}{\mu_0 \pi \lambda^2} \quad \text{Equation 16}$$

which shows that a larger λ gives smaller value of lower critical field. The upper critical field where the tubes are too dense and their individual coherence length overlap making it unable to sustain the superconducting current can be expressed in terms of coherence length as,

$$H_{c2} = \frac{\phi_0}{\mu_0 \pi \xi^2} \quad \text{Equation 17}$$

2.4 High Temperature Superconductors

The BCS theory imposes a limitation to the highest achievable superconducting temperature to be no more than 30 K. However, the discovery of cuprate perovskite superconductors overcame that limitation marking the superconducting temperature more than that of boiling point of liquid nitrogen. As the BCS theory cannot explain the phenomena at this high temperature, some other attempts have been made^{47, 48}. Weak coupling theory has been suggested which predicts that the

superconductivity arises due to the antiferromagnetic spin fluctuations⁴⁹. Theories have been evolved to go beyond the BCS theory of electron-phonon coupling predicting some other mechanisms involving *d-wave* pairing and extended *s-wave* pairing instead of conventional *s-wave* pairing. Mainly, cuprates and iron-based superconductors are found and studied in detailed manner. Cuprates are predicted to be superconducting due to the movement of electrons in copper oxide layer. Iron based superconductors also have caught great attention lately.

2.5 Heusler Superconductors

A class of alloys containing transition metals and main group elements in their composition with stoichiometric formula X_2YZ are called Heusler alloys named after Friedrich Heusler who discovered these alloys in 1903⁵⁰. In this stoichiometry, X is a transition metal from group VIII B or IB in periodic table and Y is also a transition metal such as Sc, Ti, Y, Zr, Nb, and Hf whereas Z represents the main group metals such as B, Al, Ga, and In. Due to their exotic physical properties, they have become one of the most studied intermetallic compounds for electrical and magnetic properties⁵¹. Figure 2.10 shows the periodic table of elements with possible combination to form Heusler alloys.

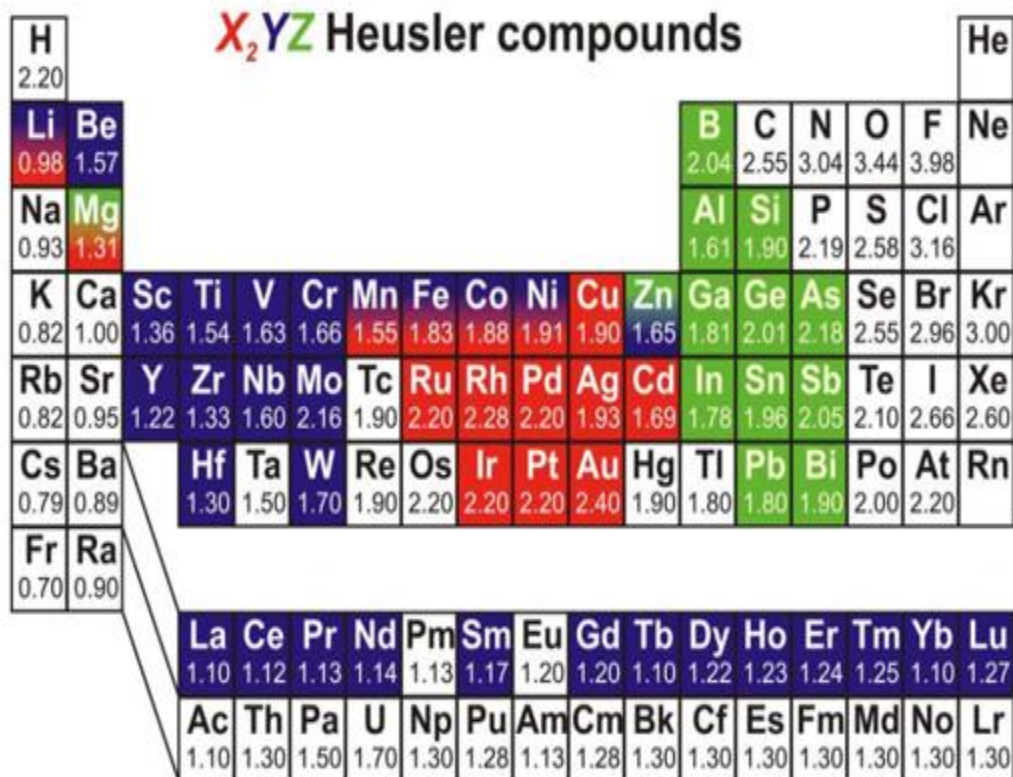


Figure 2.10 Elements forming Heusler alloys [52]

The Heusler compounds exhibit several interesting properties among which superconductivity at low temperatures for selected compounds is one of the most rigorously studied. Until now, there are 28 compounds in this family that are found to be superconducting some of which are listed in table 1 below.

Table 1 Some Heusler compounds with their T_c

Sample name	T _c (K)	Reference
YbPd ₂ Sn	2.46	53
ZrNi ₂ Al	1.38	54
ScPd ₂ Pb	2.4	55
NbNi ₂ Ga	1.54	56
ZrPd ₂ Al	3.2	57

The crystal structure of Heusler alloys is a cubic L2₁ type as shown in Figure 2.11. There are four interpenetrating face centered cubic sub-lattices A, B, C, and D in which the atoms are occupied at Wyckoff positions (0,0,0), ($\frac{1}{4}, \frac{1}{4}, \frac{1}{4}$), ($\frac{1}{2}, \frac{1}{2}, \frac{1}{2}$), and ($\frac{3}{4}, \frac{3}{4}, \frac{3}{4}$).⁵⁸

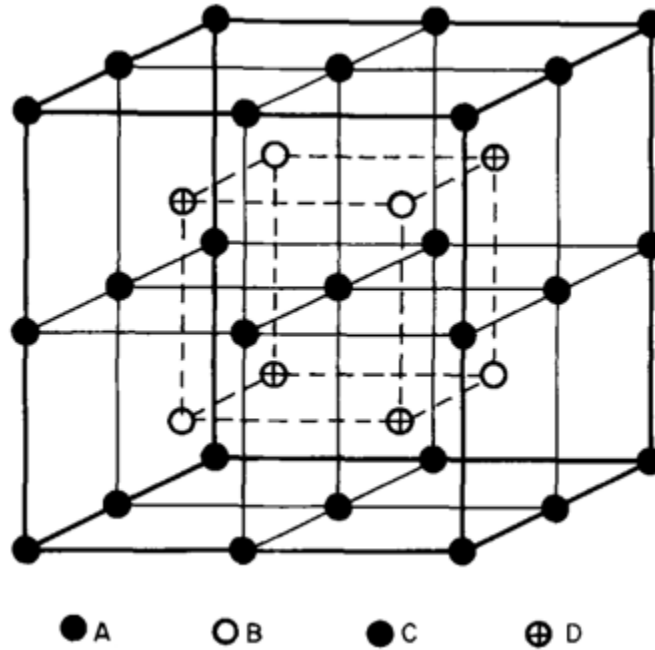


Figure 2.11 L₂₁ cubic structure of a Heusler alloy [59]

A simple recipe has been proposed to find Heusler superconductors, which involves correctly choosing three different metals with a transition metal of high electronic density of states. Ferromagnetic elements are generally avoided and the ratio of valence electrons per atom should count close to 5 or 7 according to Matthias rule^{60, 61}. Furthermore, the compounds with the number of electrons in their valence band equal to 27 are predicted to be superconducting. Heusler compounds have been found to be superconducting at a relatively low temperature in the periphery of liquid helium boiling temperature with the highest T_c being 4.9 K in YPd₂Sn⁵¹. YbPd₂Sn and ErPd₂Sn have been found to be superconducting and also surprisingly exhibit the long-range magnetic ordering at the same state^{62, 50}.

All the Heusler compounds exhibiting superconductivity are found to have a high density of states that results from the flat bands forming Van Hove singularity near the Fermi surface. The two-dimensional electronic band structure calculation as shown in fig for ZrNi₂Ga shows that the L point of Brillouin zone intersects the saddle point just above the fermi level results in maximum density of states.

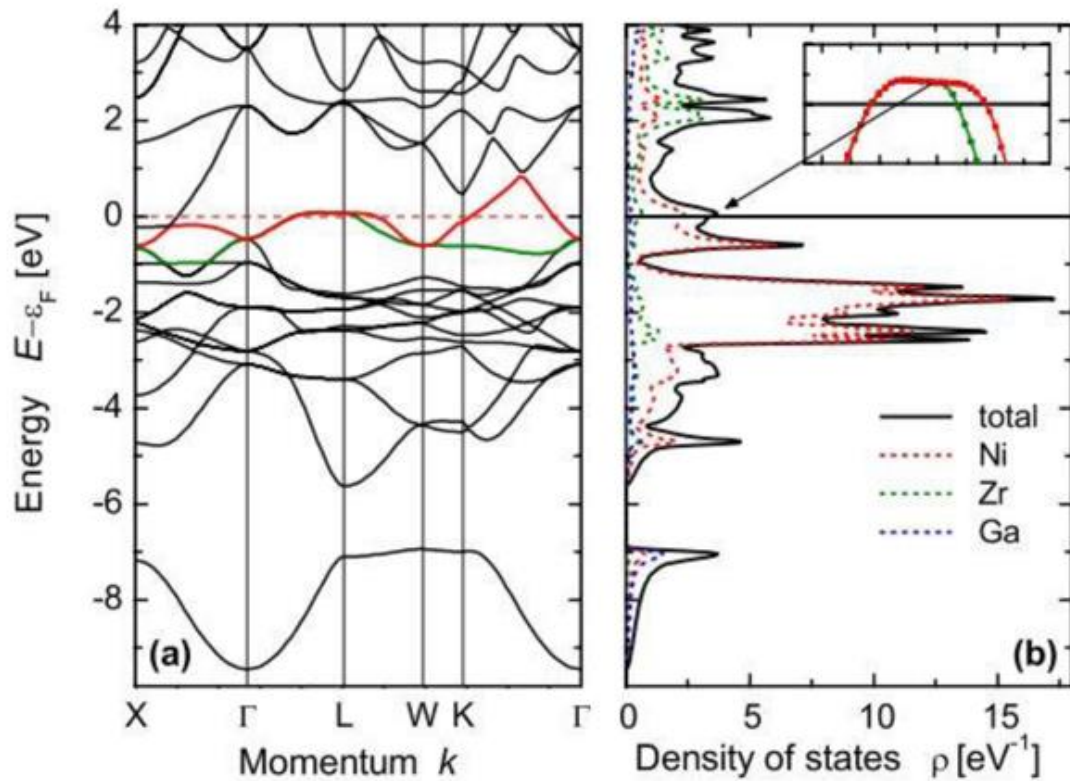


Figure 2.12 Electronic band structure (a) and the density of states (b) of ZrNi₂Ga with Van Hove singularity in inset of (b) [11]

Chapter 3: Experimental Methods

The experimental research performed in this thesis project includes sample preparation and characterization. The samples were prepared by arc melting and annealing techniques and the crystalline characterizations were performed by x-ray diffraction measurements. The samples were also subjected to magnetization, ac susceptibility and resistivity measurements. A brief description of the experimental methods employed in this research project is presented in this chapter.

3.1 Sample Preparation

The $\text{ZrNi}_{2-x}\text{Cu}_x\text{Ga}$, $\text{ZrNi}_{2-x}\text{Co}_x\text{Ga}$ ($0.05 \leq x \leq 0.25$) and $\text{ZrNi}_2\text{Ga}_x\text{Al}_{1-x}$ ($x = 0.25, 0.5, 0.75, 1.0$) alloys ($\sim 2\text{g}$ each), with the respective stoichiometry, were fabricated by standard arc-melting technique. This technique involves the formation of an electric arc between a needle-like cathode and a cathodic metal plate with the aid of high-current and low-voltage inside a sealed chamber. The chamber is pumped down to a pressure of 60 milliTorr and a partial argon pressure is introduced before the melting is carried out. Once the electric arc is turned on, a blue jet of argon plasma is formed. This extremely hot plasma jet melts the sample elements forming an intermetallic polycrystalline ingot. The anode plate (Copper) and the cathodic needle (Tungsten) are continuously water-cooled in this process to prevent them from melting.

The nickel pieces (99.98% purity), Aluminum pieces (99.99% purity), and zirconium pieces (99.95% purity) were obtained from Alfa Aesar, while the Gallium pieces (99.999% purity) were obtained from Materion. The elements were melted in stoichiometric proportion in high purity Argon atmosphere, and for homogeneity, the samples were flipped and re-melted at-least three times. The melted samples were re-measured, and the melting loss was found to be less than 0.5%. To enhance the homogeneity and the crystal structure, the melted samples were annealed in a high temperature furnace at 1073 K for two weeks followed by quenching in cold water.

3.2 Structural Characterization and Analysis

X-ray diffraction is one of the widely used techniques for the identification of crystalline phases of materials and for quantitative phase analysis. The structure of the prepared samples was investigated through powder x-ray diffraction technique. The basic physics related to this technique is discussed below.

3.2.1 X-ray Diffraction Theory

X-rays are electromagnetic radiations that can interact with the electrons in atoms. When an x-ray strikes an electron, it produces secondary spherical waves. When x-rays are shined on a crystalline material, which can be visualized as a regular array of atoms, their interaction with the electrons result in the production of spherical waves of scattered x-rays most of which cancel out by the process of destructive interference. Under certain conditions, the scattered x-rays may interfere constructively in certain directions. Bragg's law defines these conditions, as follows:

$$2d\sin\theta = n\lambda$$

In this equation, the spacing between the diffracting planes, d , can be determined by the known values of x-ray wavelength λ , and the incident angle θ relative to diffracting crystal plane. The x-ray beams which penetrate through the crystal planes produce several orders of reflection and those obeying Bragg's law interfere constructively when the path difference is equal to the integer multiple of the x-ray wavelength used. A pictorial representation of this law is shown in Fig. 3.1.

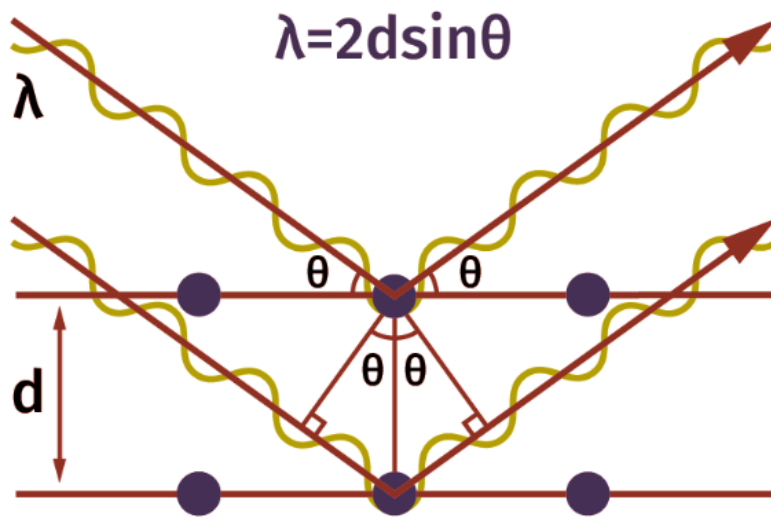


Figure 3.1 Schematic representation of Bragg's law [63]

As suggested by Bragg's law, in order to get a significant diffraction pattern, the interplanar distance between the diffracting planes should be comparable to the wavelength of incident radiation. Most of the crystals have the same order of spacing “ d ” as that of the x-ray wavelength that has a magnitude of few angstroms. The wavelength of the x-ray used in this experiment was of Cu $K\alpha$ radiation equal to 1.54 Å.

3.2.2 X-ray Diffractometer

An x-ray diffractometer is used to analyze the diffraction pattern when the sample is exposed to the x-ray beams. The experimental setup consists of a source producing x-ray, a high-voltage power supply, a monochromator to filter the desired wavelength, a target sample to be studied and a detector. The one that was used in this experiment is shown in Figure 3.2.



Figure 3.2 Scintag x-ray diffractometer

The main components of x-ray diffractometer are shown in Fig. 3.3. The x-ray source generates the radiation which is shined on the surface of a powder sample and the diffracted beams are detected by a detector positioned according to the incident angle of radiation.

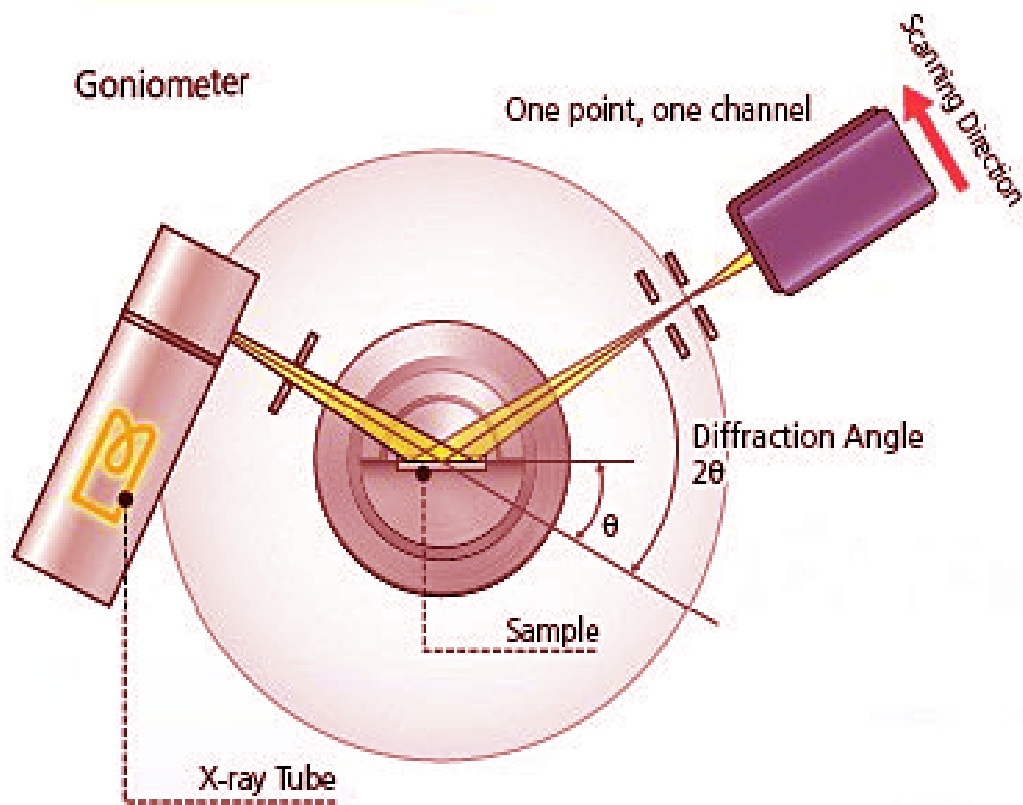


Figure 3.3 Components of an x-ray Diffractometer [64]

3.2.3 X-ray Diffraction Analysis

X-ray diffraction provides information on crystal structure, structural parameters, and crystalline phase of the materials. The distribution of the atoms within the lattice determines the peak intensities at specific angles as determined by Bragg's law. The phase identification is done by matching the x-ray diffraction pattern database provided by International Center for Diffraction Data (ICDD). To determine the structural phases and parameters of the samples, the raw data from diffraction measurement were analyzed using Powdercell⁶⁵, a diffraction data analysis software.

3.3 Compositional Characterization and Analysis

The composition of the sample was characterized by Scanning Electron microscopy (SEM) using Zeiss Supra 35 VP FEG microscope, courtesy of the Miami University Center for Advanced Microscopy and Imaging.

3.3.1 Scanning Electron Microscopy: Theory

When high energy electron beams hit the atoms, the electrons and nucleons of the atom get excited and produce various signals through elastic and inelastic scattering. These interactions produce secondary electrons and backscattered electrons. These signals can be used to collect information about the surface topology and composition of the material. The scanning electron microscope is designed such that it can collect the signals from the secondary electrons and the backscattered electrons.

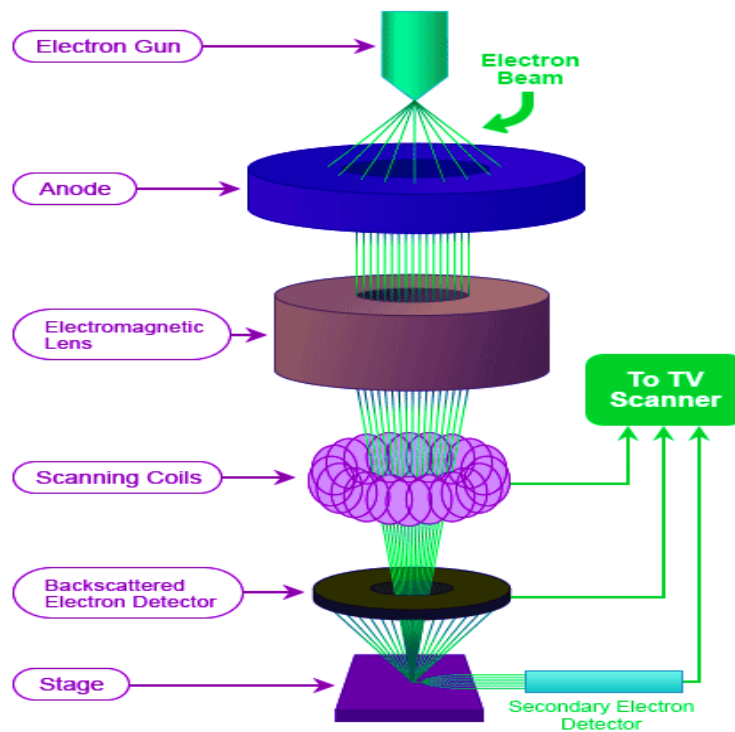


Figure 3.4 Components of Scanning Electron Microscope (SEM) [66]

The major components of Scanning Electron Microscope are as shown in Figure 3.4. The electron source, a tungsten crystal, generates electrons which are accelerated by the aid of high voltage between the crystal and an anode. The electron beams are then allowed to pass through electromagnetic lens and narrowed through scanning coils to focus on the sample. There are additional electromagnetic coils which scan the electron beam across the sample. There are separate signal detectors for detecting secondary electrons and reflected electrons. These detectors project the signals to the screen as images. The reflected electrons will show the composition and the secondary electrons will show the topography of the sample.

In determining compositional contrast, the signals from backscattering are useful. Backscattered electrons (BSE) are produced when the incident electron gets scattered back by the positively charged nucleus. The number of BSE depends on the size of the nucleus. So, the intensity of BSE offers a good insight in the composition of the sample. The charge signal from the BSE is detected by a quadrant silicon detector photo-multiplier system which is placed directly above the sample as the BSE electrons are scattered almost antiparallel to the incident electron beam. In general, the Heusler alloys with off-stoichiometry show phase segregation which can also be observed in XRD data analysis.

3.3.2 Energy-Dispersive X-ray Spectroscopy

Each characteristic x-ray has a different wavelength associated with it. The energy to create this characteristic x-ray goes on increasing for heavier elements due to higher cohesive force. So, these characteristic spectra can be used to observe the proportion of elements present in a sample. The characteristic spectra are collimated and transmitted to a detector in a different assembly within the SEM. The detected signal is quantified as a plot of intensity versus energy. The quantified values can be used to determine the accuracy of the sample fabrication by comparing with the predicted values. An EDS unit in Zeiss Supra 35 was used to detect the characteristic x-rays.

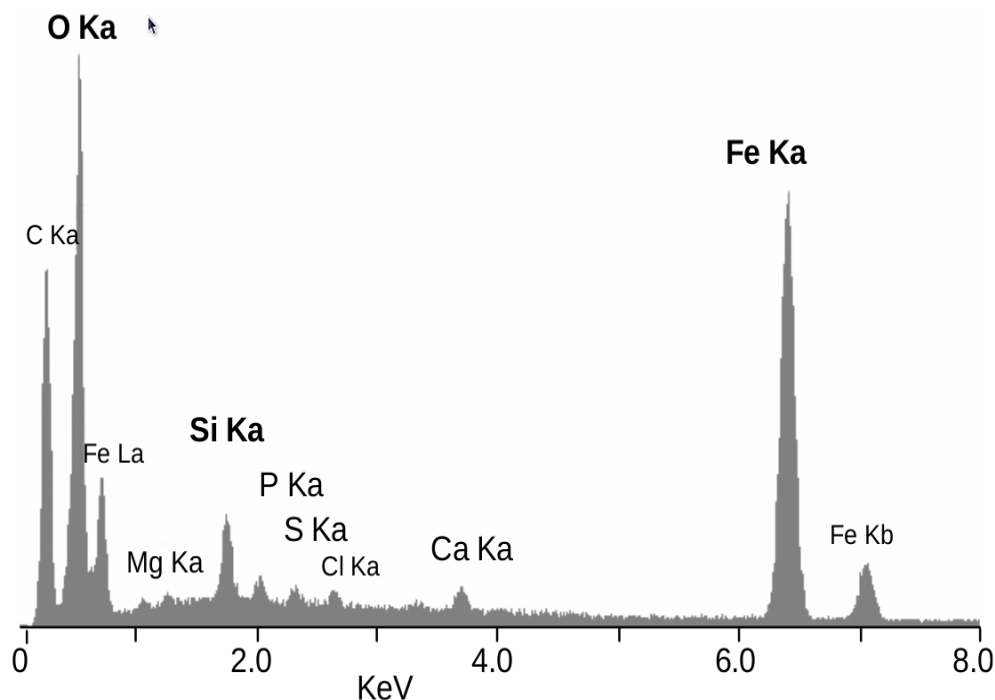


Figure 3.5 EDS spectrum showing various transitions [67]

3.4 Resistivity and Magnetization Measurement

For the purpose of measuring resistivity and magnetization, the Physical Property Measurement System (PPMS) made by Quantum Design Inc. was used.

The magnetization measurements were carried out using the vibrating sample magnetometer (VSM) option. A temperature range of 2 K – 10 K and applied field of 25 Oe was used to obtain magnetization versus temperature, M-T, data. The sample was cooled down to 2 K to record zero field cooled (ZFC) data in absence of external magnetic field and after the temperature stabilized at 2 K, the desired magnetic field was applied to obtain the M-T data. Field Cooled Cooling (FC) data were obtained by applying magnetic field while cooling from 10 K to 2 K. The magnetization versus applied magnetic field (M-H) data were measured at 2 K in an applied magnetic field range of -10 kOe to 10 kOe. To measure the ac susceptibility as a function of temperature, χ -T, the ACMS option in the PPMS was used and the measurement was carried out in a temperature range of 2 K-10 K. The frequencies of 50 Hz, 100 Hz, 1000 Hz, 5000 Hz and 10000 Hz were used under

an ac magnetic field of 10 Oe. The resistivity data with variation of temperature, ρ -T, were obtained using the PPMS through resistivity option. A standard four probe technique was used

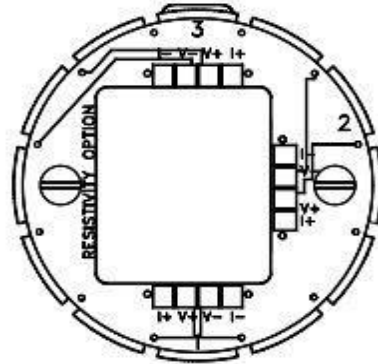


Figure 3.6 Resistivity puck [68]

where four electrical contacts were made on a thin rectangular piece of sample mounted on a resistivity puck (shown in fig). The four leads of the resistivity puck were connected to the four electrical contact points of the sample. There are two current leads, I+ and I-, through which the current flows and two voltage leads, V+ and V-, across which the potential is measured. The resistivity as a function of temperature was measured in the PPMS in the range of 2 K-300 K. The resistivity versus applied magnetic field, ρ -H, was measured in the field range of -10 kOe to 10 kOe at a temperature of 2 K.

3.4.1 The Physical Property Measurement System

The PPMS is a complex multifunctional device which can measure resistivity, ac and dc magnetization, torque magnetization and other thermal and electrical properties. A measurement is carried out through the installation of applicable experimental option and setting up an automated sequence specific for that measurement. The PPMS can be operated in a wide range of temperature variation (1.75 K – 400 K) and applied magnetic field variation (up to 90 kOe). The high magnetic field is produced within the PPMS by a superconducting magnet. In order to operate the PPMS liquid helium and liquid nitrogen are used as coolant and a desirable low temperature is achieved. To monitor the sample temperature, there is a platinum resistance thermometer which reads the temperatures from 80 K to 400 K and a negative temperature coefficient thermometer

which reads temperatures between 1.75 K and 100 K. Both the thermometers are connected below the electrical connectors of the sample puck.

Hardware Components of PPMS

The major components of the PPMS are as follows:

1. Dewar
2. Probe
3. Model 6000 PPMS Controller
4. Vacuum Pump
5. Electronic Cabinet
6. Sample Puck and Assorted Tools

The schematic diagram of the components of PPMS is shown below.

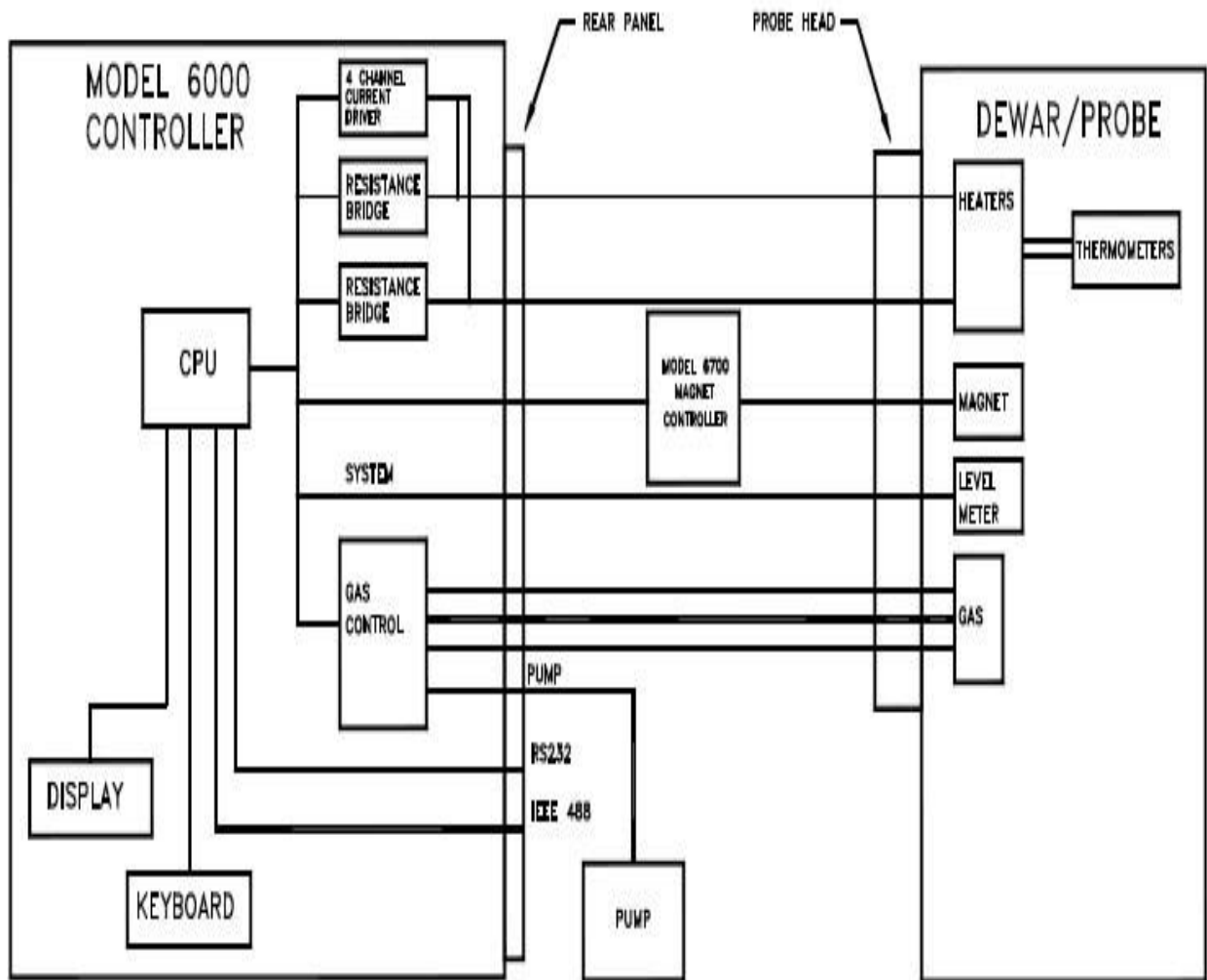


Figure 3.7 Block Diagram of PPMS [68]

1. Dewar

The dewar contains a liquid helium bath surrounded by a jacket where nitrogen is filled occasionally. The liquid helium is transferred from an external helium recovery and liquefaction plant. As the liquid helium boils at 4.2 K, the liquid nitrogen whose boiling point is 77 K reduces the boiling rate of helium thereby preserving the helium in liquid state inside the dewar. The helium gas that is boiled off is pumped out by a dry scroll pump which is connected to the helium recovery plant for liquefaction.

2. Probe

The probe consists of the basic temperature control hardware, the helium level meter, the superconducting magnet, the sample puck connectors, the gas lines, helium impedance tube, and electronic connections. It is immersed in the helium bath so as to keep the probe components cool all the time. The center of the probe consists of a vacuum tube which encloses the experimental apparatus. The base of the probe has a 12-pin connection through which the experimental apparatus communicates with the Model 6000 PPMS controller. The helium impedance tube connects the dewar with the cooling annulus which is an evacuated region between the sample chamber and the inner vacuum tube. The impedance tube supplies helium to the cooling annulus so that it can vary the temperature of the sample chamber evenly. The helium flow from the dewar to the cooling annulus is regulated and controlled by the impedance assembly. The electrical connections to the magnet and impedance assembly is contained in the baffled rods which run through the length of the probe. On the exterior of the probe is the niobium-titanium superconducting coil immersed in the liquid nitrogen bath such that the coil remains in the superconducting state all the time. The superconducting coil is oriented such that the magnetic field produced whenever a current flow through the circuit is along the long axis of the sample area. The external current source is disconnected by using a persistent switch once the desired magnetic field is established by the means of the persistent current. A magnetic field of about 90 kOe is produced by flowing 50 Ampere current.

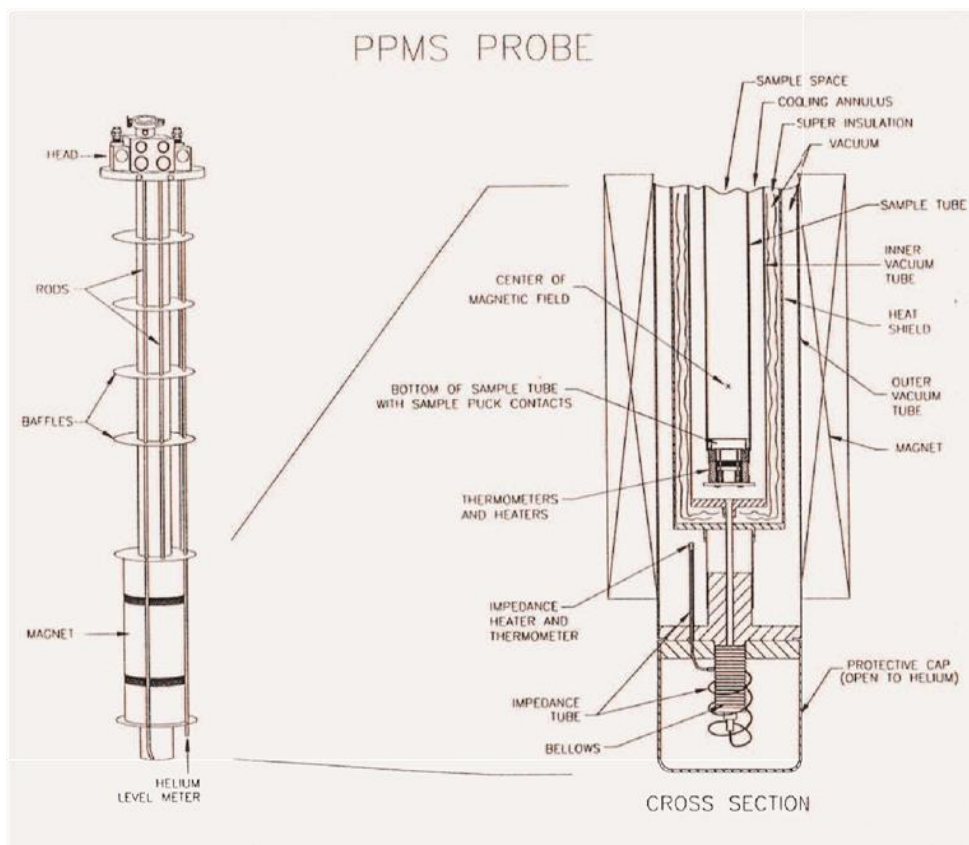


Figure 3.8 Components of the PPMS Probe [68]

3. Model 6000 PPMS Controller

It is an integrated user interface containing a CPU board, a motherboard, and a system bridgeboard. There are also the gas valves and gas lines which are used to control temperature.

4. Vacuum Pump

A direct drive vacuum pump is installed in the bottom of electronics cabinet which operates to control the sample chamber pressure and temperature. The gas flow rate and the vacuum are regulated by the valves in the Model 6000 controller. In order to avoid contamination, a foreline trap on the input side and an oil-mist filter on the exhaust line are attached.

5. Electronics Cabinet

The electronics cabinet contains the Model 6000 controller, a power strip, and the vacuum pump with some space for additional hardware and other electronics that are needed for some PPMS options.

6. Sample Puck and Assorted Tools

The sample puck holds the samples for the experiments which can be inserted inside the sample chamber. There are some assorted tools such as insertion rod, adjustment tool and wiring testing tool used for proper handling and testing of the puck functioning.

The Software used in the PPMS is called PPMS MultiVu which is a windows-based control software which enables the PPMS to create an automated sequence command and control the system parameters like temperature and magnetic field.

3.4.2 Vibrating Sample Magnetometer (VSM)

The VSM is a very sensitive device available for PPMS that measures the magnetic properties of the sample. The VSM is capable of measuring precisely the magnetic moment and is very sensitive to a significantly small moment changes which can detect as low as 1 millionth emu of magnetic moment change. The magnetic moment as a function of parameters like temperature and magnetizing field are measured accurately through VSM. For all the magnetic measurements in this thesis project, the VSM made by quantum design was used which is compatible with the PPMS and could be installed manually.

As the name suggests, in the VSM, the sample is oscillated perpendicularly to the applied magnetic field produced by the superconducting coil. There is a pickup coil within the sample area where the sample vibrates between its center points. The main parts of VSM are the linear motor head which vibrates the sample, an external coil set assembly for detection which is inserted into the sample chamber, and the electronic setups for driving the linear motor and detection of the signals. The MultiVu software automates and controls the whole VSM-PPMS functions.

The VSM operates in accordance with Faraday's law for electromagnetic induction. The induced voltage in the coil can be mathematically expressed as,

$$V_{induced} = \frac{d\Phi}{dt} = \frac{d\Phi}{dz} \frac{dz}{dt}$$

Where, Φ is the magnetic flux induced in the pickup coil, z is the vertical distance from the sample to the coil, and t is the time. The voltage of the sinusoidally oscillating sample is given through the following relation;

$$V_{coil} = 2\pi f C m A \sin(2\pi f t)$$

Where, f is the frequency of sample oscillation, C is the coupling constant, m is the dc magnetic moment, and A is the amplitude of sample oscillation. The VSM used is capable of oscillating the sample by default at a frequency of 40 Hz.

The magnetic moment measurement is acquired through the measurement of coefficient of the sinusoidal voltage response from the detection coil. The sample is driven sinusoidally with the center of oscillation at the vertical center of pickup coil. The VSM motor module controls the position and amplitude of oscillation.

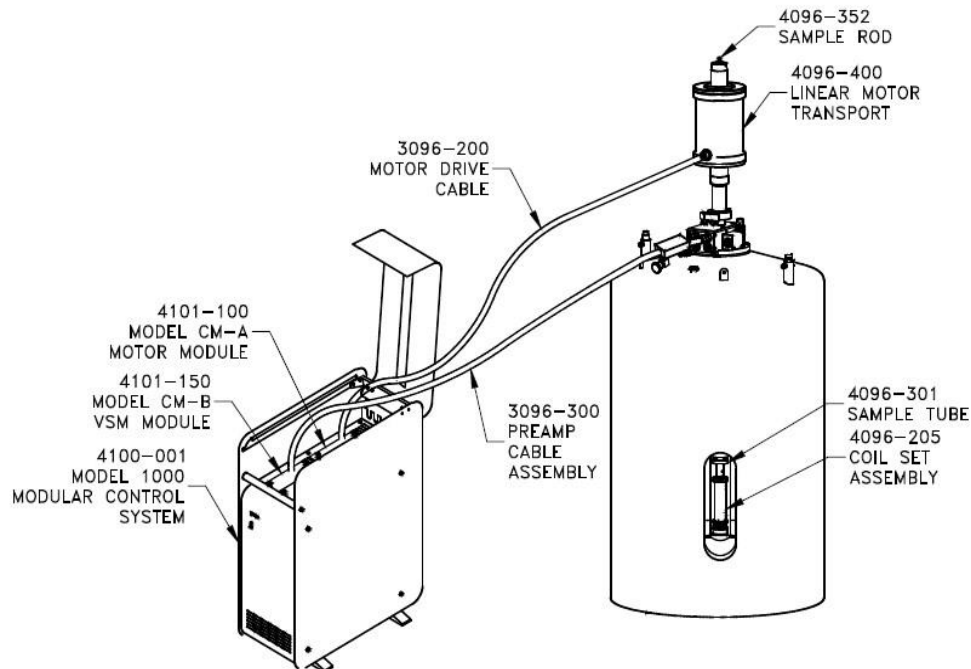


Figure 3.9 Components of VSM-PPMS system [68]

3.4.3 AC Magnetometer

The AC magnetometer is a device used to perform the ac susceptibility measurements of the sample. It uses the AC magnetic field to create time dependent moment. A current is set up in the pickup coil due to the field of time dependent moment. In this case, the sample measurement is carried out without the sample being in motion unlike the VSM. The AC measurement provides information about the magnetization dynamics. At higher frequencies, the magnetization of the sample lags behind the drive field yielding the phase difference, ϕ , relative to the drive signal in addition to the magnetic susceptibility, χ . So, there is an in-phase or the real component of susceptibility, χ' , and an out of phase or the imaginary component of the susceptibility, χ'' . In this project, the ACMS was used to show the frequency dependence of the superconducting transition temperature of the selected samples.

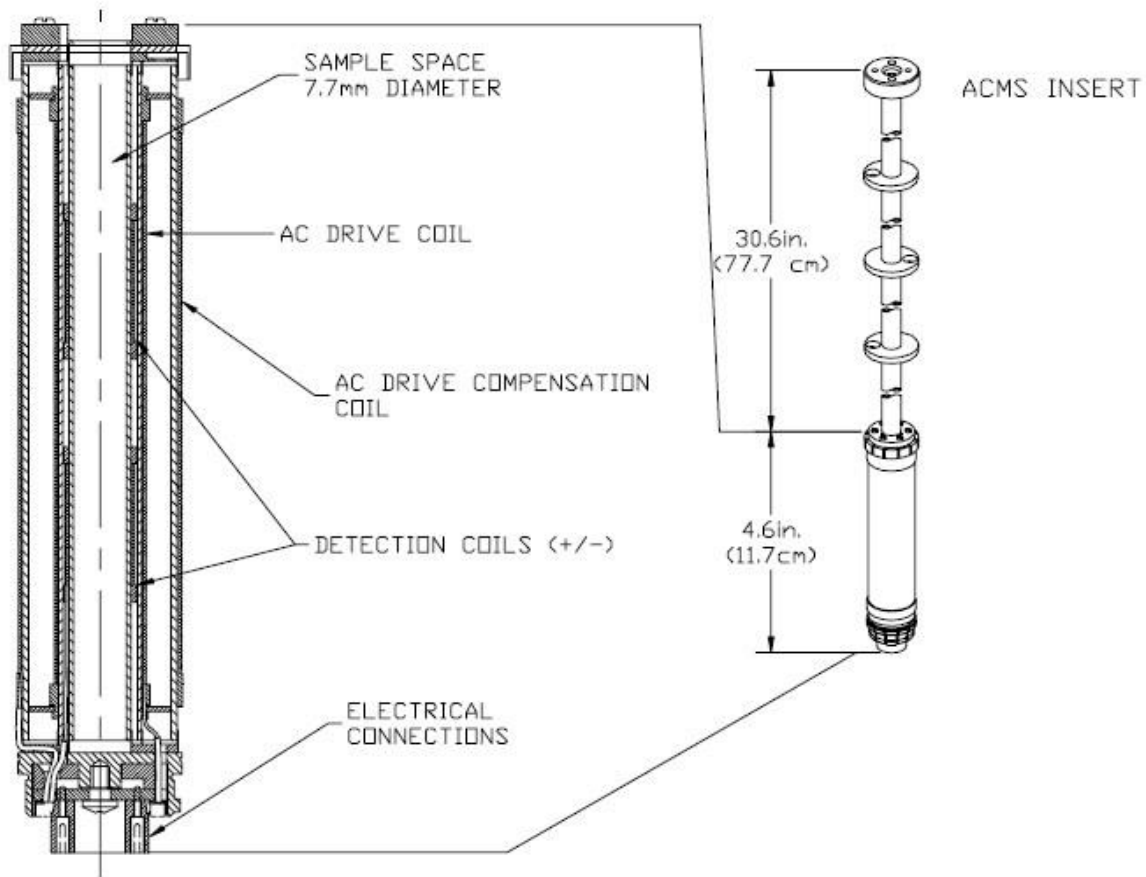


Figure 3.10 ACMS parts and cross-sectional view of coil [68]

Chapter 4: Results and Discussion

In this chapter, all the experimental results and possible explanations behind the observed results are described. Several Heulser alloys were fabricated and prepared. Magnetic and electrical resistivity measurements were performed on all the samples. The $\text{ZrNi}_{2-x}\text{TM}_x\text{Ga}$ ($0.05 \leq x \leq 0.25$) and $\text{ZrNi}_2\text{Ga}_{1-x}\text{Al}_x$ ($x=0.25, 0.5, 0.75, 1$) samples were fabricated and characterized. Table 2 and Table 3 show the list of the samples.

Table 2 A list of $\text{ZrNi}_{2-x}\text{TM}_x\text{Ga}$ samples.

$\text{ZrNi}_{2-x}\text{Cu}_x\text{Ga}$	$\text{ZrNi}_{2-x}\text{Co}_x\text{Ga}$	X
$\text{ZrNi}_{1.95}\text{Cu}_{0.05}\text{Ga}$	$\text{ZrNi}_{1.95}\text{Co}_{0.05}\text{Ga}$	0.05
$\text{ZrNi}_{1.9}\text{Cu}_{0.1}\text{Ga}$	$\text{ZrNi}_{1.9}\text{Co}_{0.1}\text{Ga}$	0.1
$\text{ZrNi}_{1.85}\text{Cu}_{0.15}\text{Ga}$	$\text{ZrNi}_{1.85}\text{Co}_{0.15}\text{Ga}$	0.15
$\text{ZrNi}_{1.8}\text{Cu}_{0.2}\text{Ga}$	$\text{ZrNi}_{1.8}\text{Co}_{0.2}\text{Ga}$	0.2
$\text{ZrNi}_{1.75}\text{Cu}_{0.25}\text{Ga}$	$\text{ZrNi}_{1.75}\text{Co}_{0.25}\text{Ga}$	0.25

Table 3 A list of $\text{ZrNi}_2\text{Ga}_{1-x}\text{Al}_x$ samples.

$\text{ZrNi}_2\text{Ga}_{1-x}\text{Al}_x$	X
$\text{ZrNi}_2\text{Ga}_{0.75}\text{Al}_{0.25}$	0.25
$\text{ZrNi}_2\text{Ga}_{0.5}\text{Al}_{0.5}$	0.5
$\text{ZrNi}_2\text{Ga}_{0.25}\text{Al}_{0.75}$	0.75
ZrNi_2Al	1

The results and related discussion for all the measurements are provided below including structural properties, resistivity, and magnetization.

4.1 Structural properties

The structural properties of all the samples were investigated using x-ray diffraction and the phase purity and compositional variations were studied using the measurements from SEM imaging technique.

4.1.1 X-ray diffraction

Room temperature x-ray diffraction (XRD) was carried out on all powdered samples.

Figure 4.1 shows the XRD patterns for the $\text{ZrNi}_{2-x}\text{Cu}_x\text{Ga}$ and $\text{ZrNi}_{2-x}\text{Co}_x\text{Ga}$ samples, and all of them exhibit the $L2_1$ cubic structure which was determined through the indexing and refinement process. The variation of stoichiometry does not change the crystal structures significantly for both the $\text{ZrNi}_{2-x}\text{Cu}_x\text{Ga}$ and $\text{ZrNi}_{2-x}\text{Co}_x\text{Ga}$ systems. For some samples, a minor hump-like feature was observed at the base of the respective 220 peak. As shown in Figure 4.3, for the Cu doped compounds, the lattice parameters increased from 6.0867 \AA ($x = 0$) to 6.0970 \AA ($x = 0.25$), while for the Co doped compounds the lattice parameters decreased to 6.0831 \AA ($x = 0.25$). The rearrangement of the doping atoms within the lattice causes this variation in lattice parameter.

Figure 4.2 shows the x-ray diffraction patterns of $\text{ZrNi}_2\text{Ga}_{1-x}\text{Al}_x$ compounds, which also exhibit cubic $L2_1$ phase at room temperature with similar characterization peaks as Cu and Co-doped compounds with some variations in peak intensities. The lattice parameter of the samples was found to be increasing from 6.0908 \AA for $x = 0.25$ to 6.1074 \AA for $x = 1$ as shown in Figure 4.4. This can be interpreted as the takeover of the lattice site of Ga by Al atoms which have a bigger atomic radius.

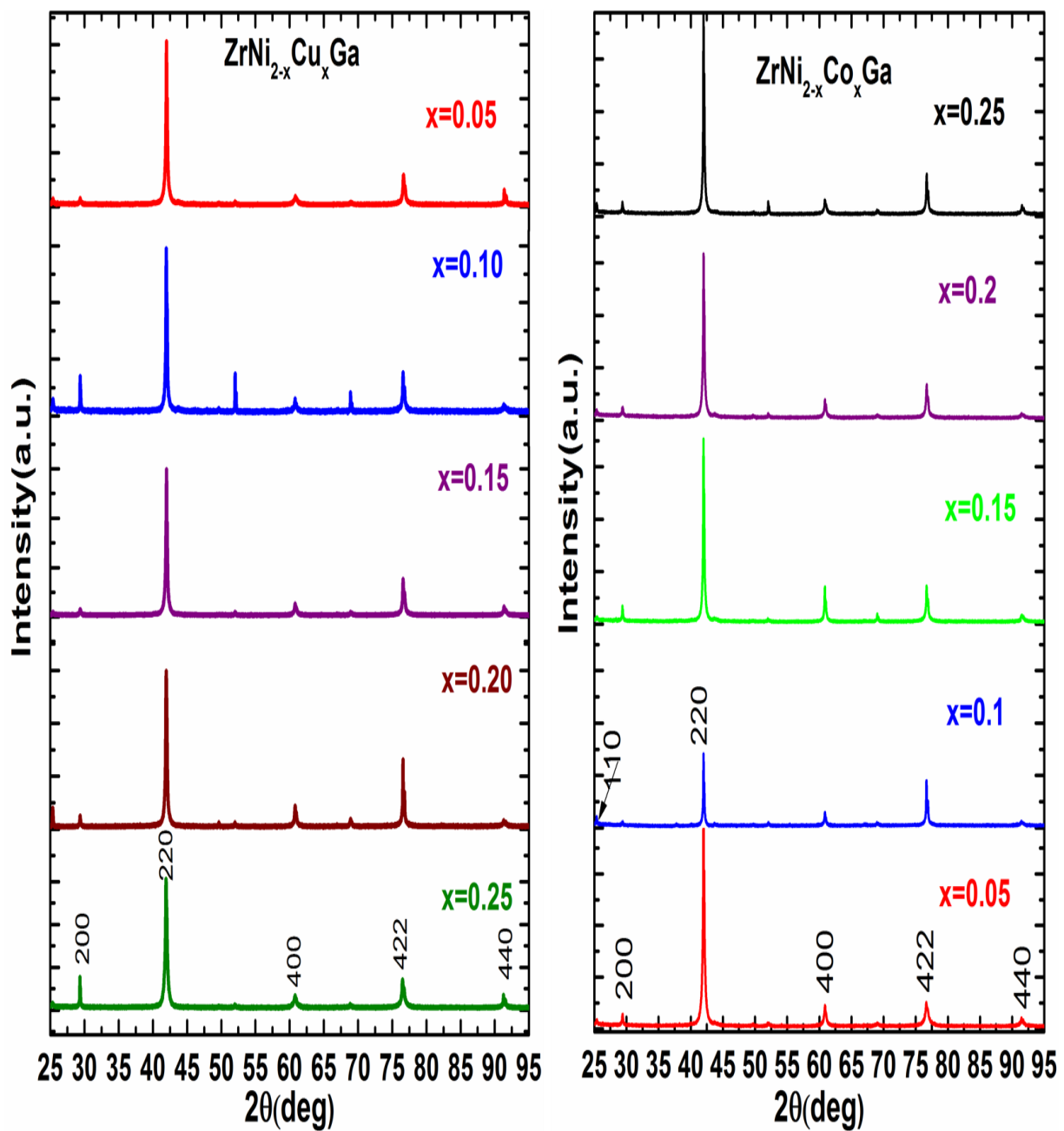


Figure 4.1 X-ray diffraction pattern of $\text{ZrNi}_{2-x}\text{Cu}_x\text{Ga}$ and $\text{ZrNi}_{2-x}\text{Co}_x\text{Ga}$ compounds

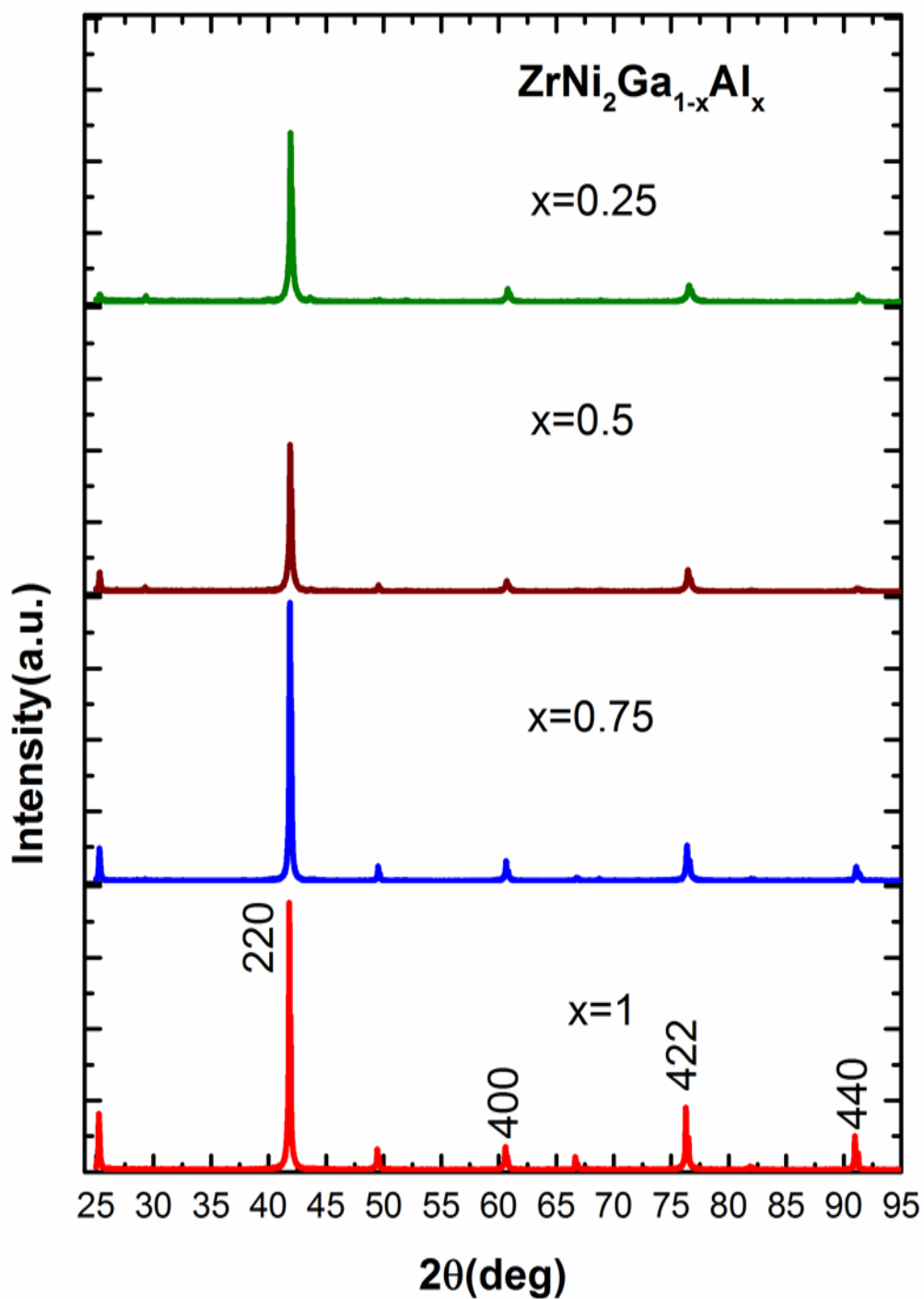


Figure 4.2 X-Ray diffraction pattern of $\text{ZrNi}_2\text{Ga}_{1-x}\text{Al}_x$ compounds

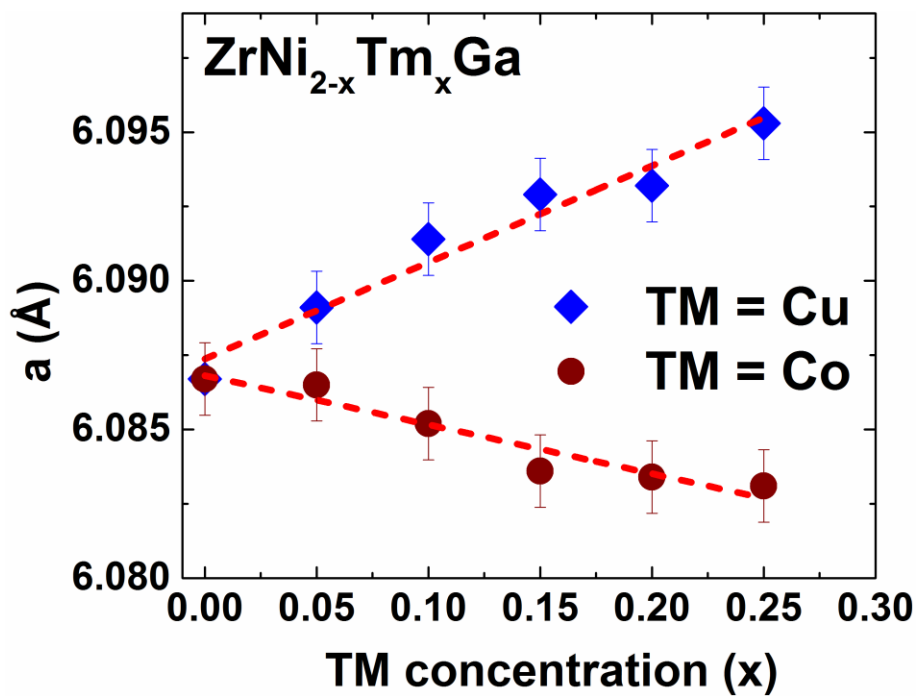


Figure 4.3 Variation of lattice parameter in Cu and Co-doped compounds

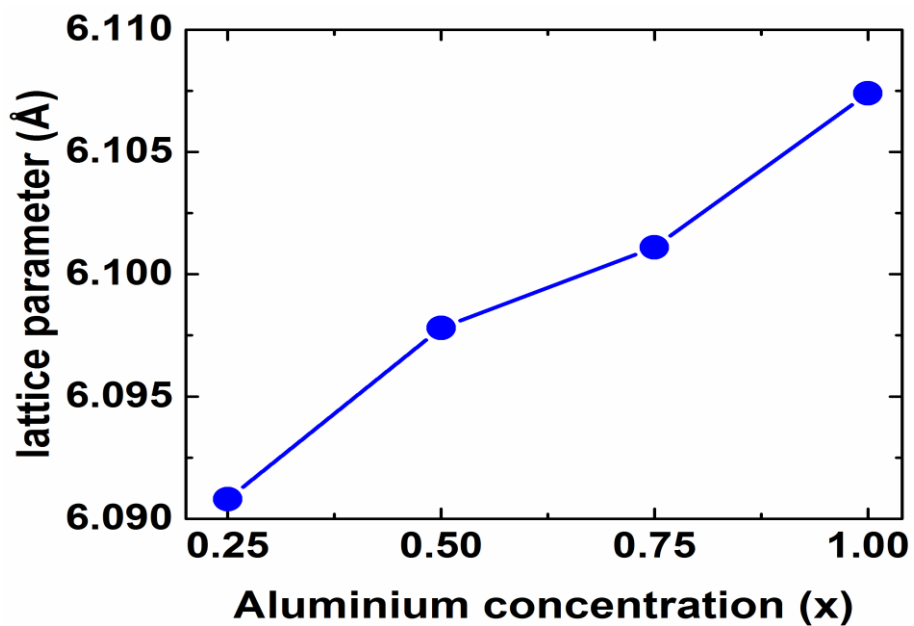


Figure 4.4 Variation of Lattice parameter in Al-doped compounds

4.1.2 Scanning Electron Microscope

Figure 4.5 and Figure 4.6 show the SEM micrographs of Cu-doped compounds and Co-doped compounds respectively at room temperature. These topographic images at 1k magnification were

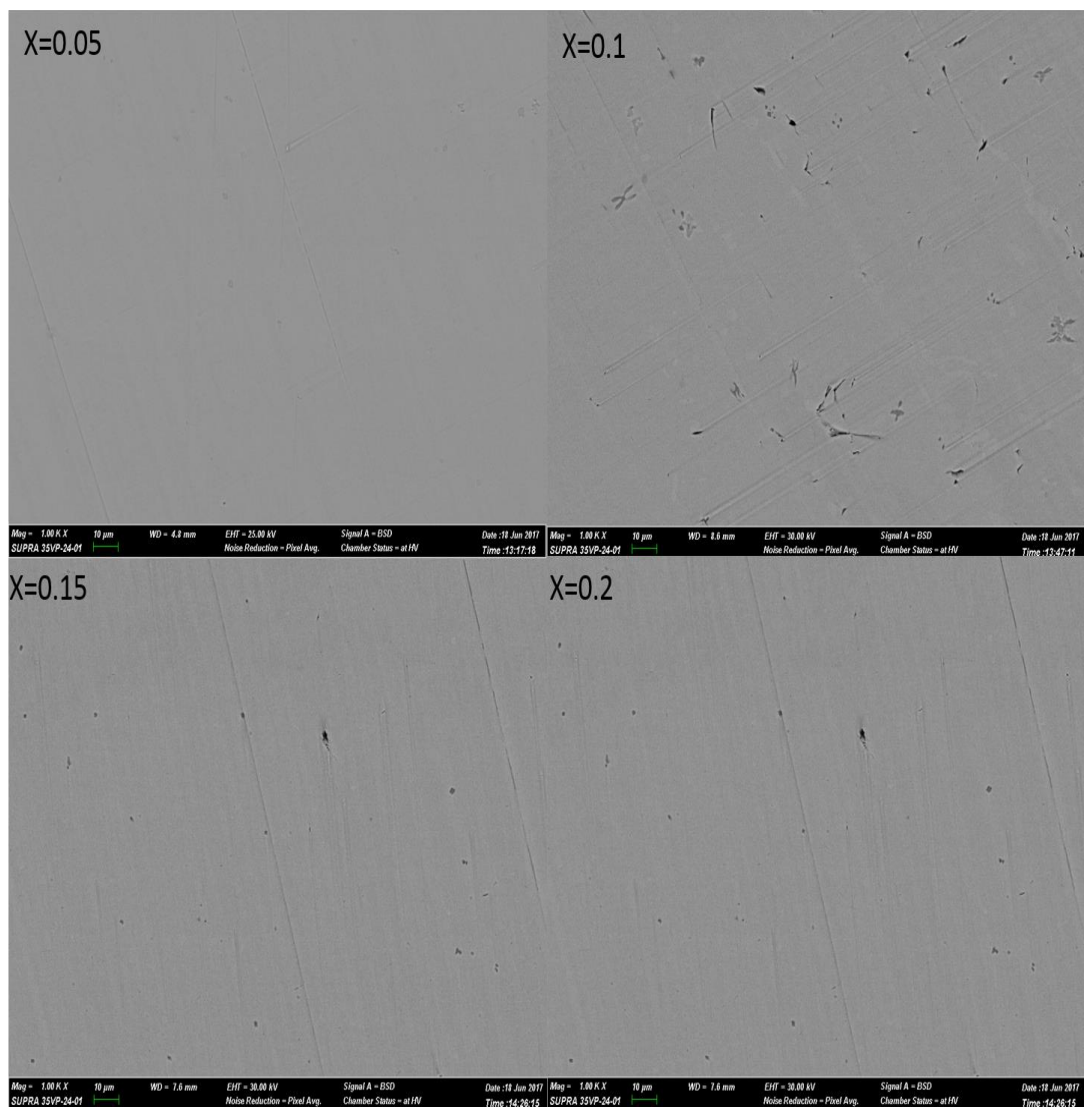


Figure 4.5 SEM images of Cu-doped compounds

obtained at 500 nm penetration from surface of the sample. The segregation of the phases was not seen as was the similar result obtained from X-ray diffraction which showed single phase for these compounds. The EDS analysis also shows the homogeneity of the samples where the targeted

stoichiometry is very close in several regions which is discussed in detail for $x=0.25$ concentration for both the Cu and Co-doped samples as in Figure 4.7.

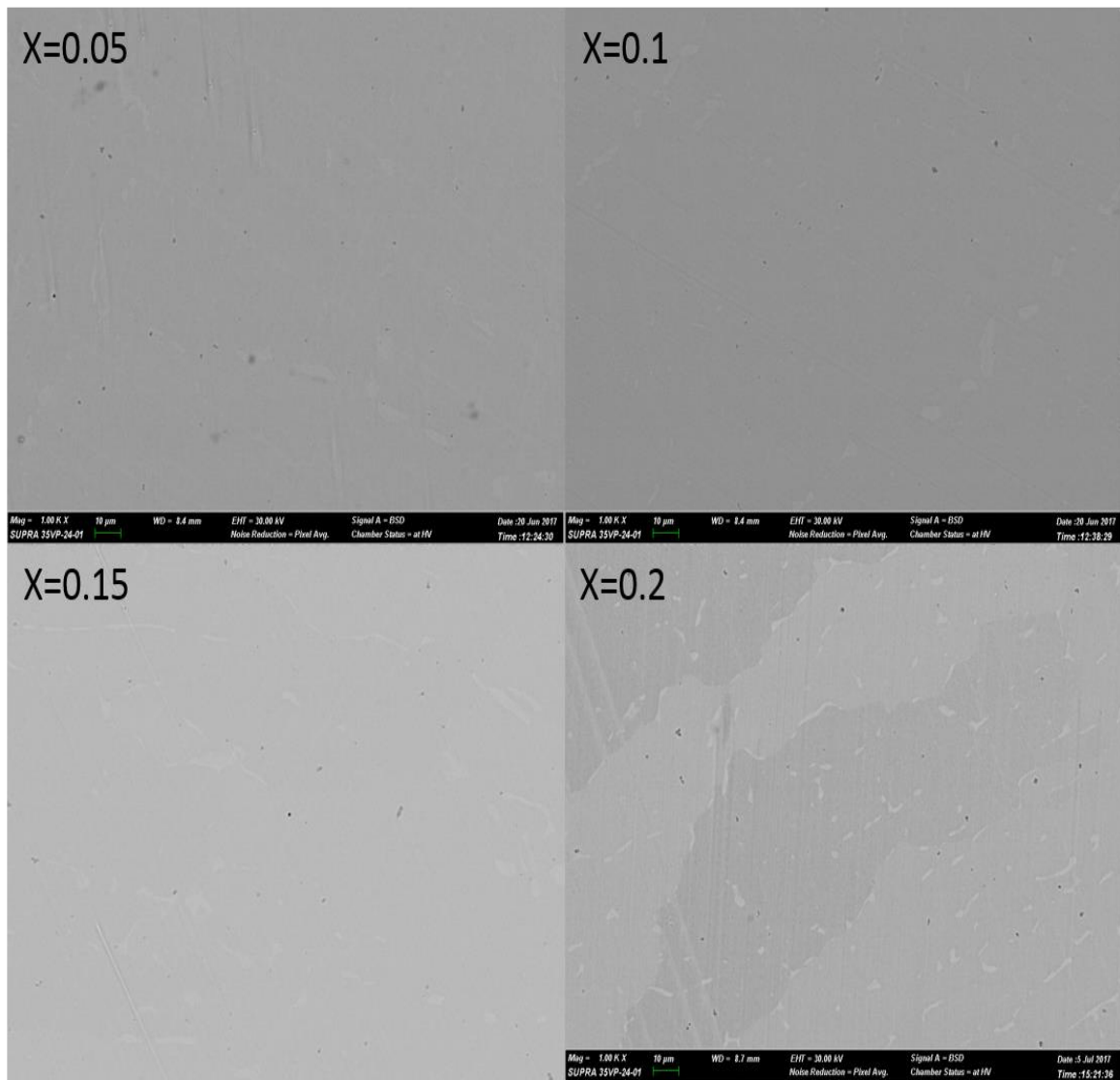


Figure 4.6 SEM images of Co-doped samples

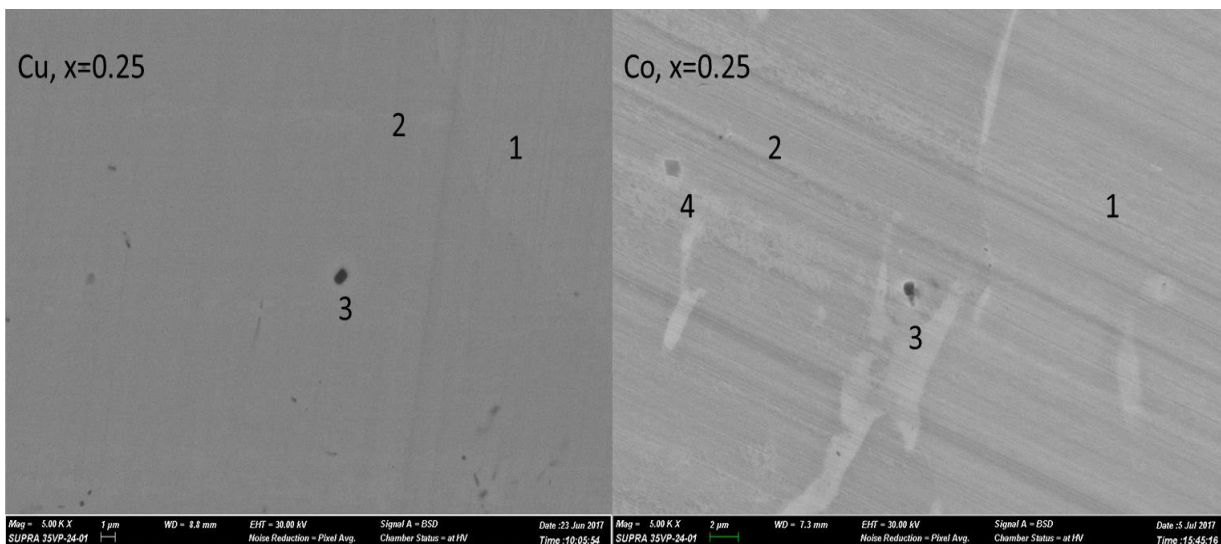


Figure 4.7 SEM micrographs of the Cu doped compounds with $x = 0.25$. (left) and Co doped sample (right) with $x = 0.25$.

A comparison of homogeneity of constituent elements in Cu-doped and Co-doped samples is shown in Figure 4.7. The SEM micrograph for the Cu doped sample with $x = 0.25$ showed two primary compositional phases (labelled 1 and 2) with nearly identical stoichiometry. The EDS analysis of the two regions suggested an average composition of 43.86% Ni, 7.9% Cu, 26.27% Zr, and 21.96% Ga. A small concentration of Zr-rich dark precipitates (labelled 3), with the composition 41.94% Ni, 7.77% Cu, 29.55% Zr, and 20.74% Ga were also observed in the sample. For the Co-rich $\text{ZrNi}_{2-x}\text{Co}_x\text{Ga}$ compounds, the SEM images showed three light grey regions and small concentrations of Zr-rich dark spots (see Fig. 4.5 (c)). While the elemental compositions of the light grey regions (marked 1 and 2 in Fig. 4.5(d)) were more similar in composition and closer to the targeted composition, region 3 showed a relatively higher concentration of Co. The dark precipitates (region 4) observed in the SEM images of the Co doped samples were Zr rich. Considering these results of the EDS analysis, the minor humps observed in the XRD data in Figure 4.1, may be most likely be attributed to the Zr-rich precipitates observed in the samples.

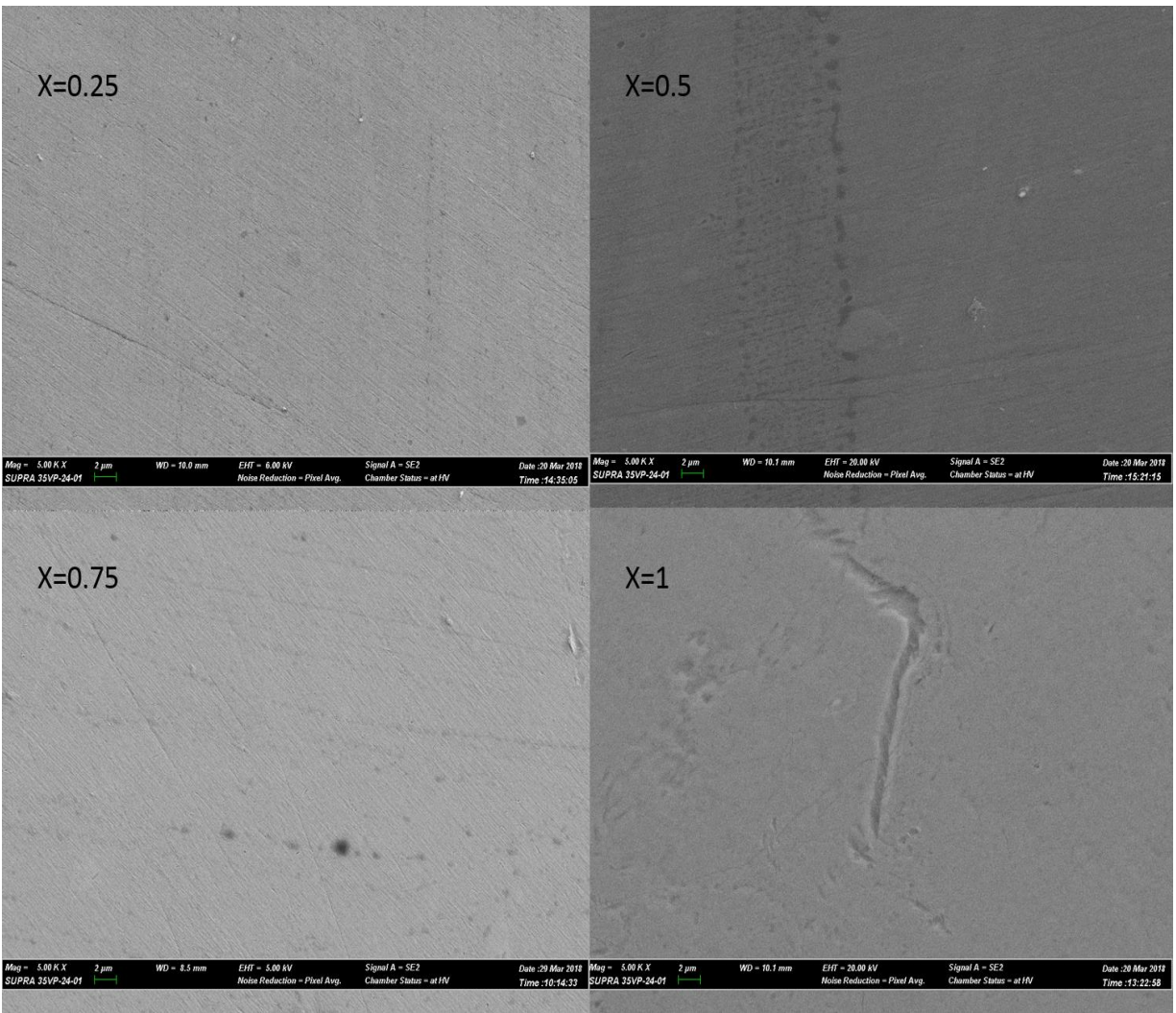


Figure 4.8 SEM images of Al-doped samples

The SEM micrographs of Al-doped compounds are shown in Figure 4.8. All the compounds showed near homogeneity in the surface structure as shown in 5k resolution imaging. The dark spots were found to be Zr-rich while the bright spots observed in some samples were found to be Ni-rich. The EDS analysis showed a very close matching in the percentage of constituent elements as predicted by the stoichiometric calculations. Although, this series of compounds showed an unusual transition above the superconducting transition, which will be discussed in resistivity and magnetization section, no foreign elements were detected for any of the samples.

4.2 Resistivity Measurements:

4.2.1 Temperature dependent Resistivity, $R(T)$

As shown in Figure 4.9, ($\rho(T)$, data), for $x \leq 0.25$, all the Cu doped compounds exhibit superconductivity below 3 K. The SC transition is signified by the sharp decrease of resistivity to zero. Although the Cu doped samples exhibit superconductivity, between 300 K and 1.8 K, all the $\text{ZrNi}_{2-x}\text{Co}_x\text{Ga}$ ($x \leq 0.25$) compounds showed normal metallic behavior as shown in Figure 4.10. No SC transition was observed even in the sample with $x \leq 0.05$, where Co is only 1.25 % of the total composition. This is unusual in light of previous conjectures linking the valence electron concentration (e/a) to the superconducting properties of Heusler compounds¹², given that Co has only one less electron than Ni and thus, e/a of the Co sample with $x=0.05$ doesn't vary significantly from that of ZrNi_2Ga (6.7375 versus 6.75, respectively).

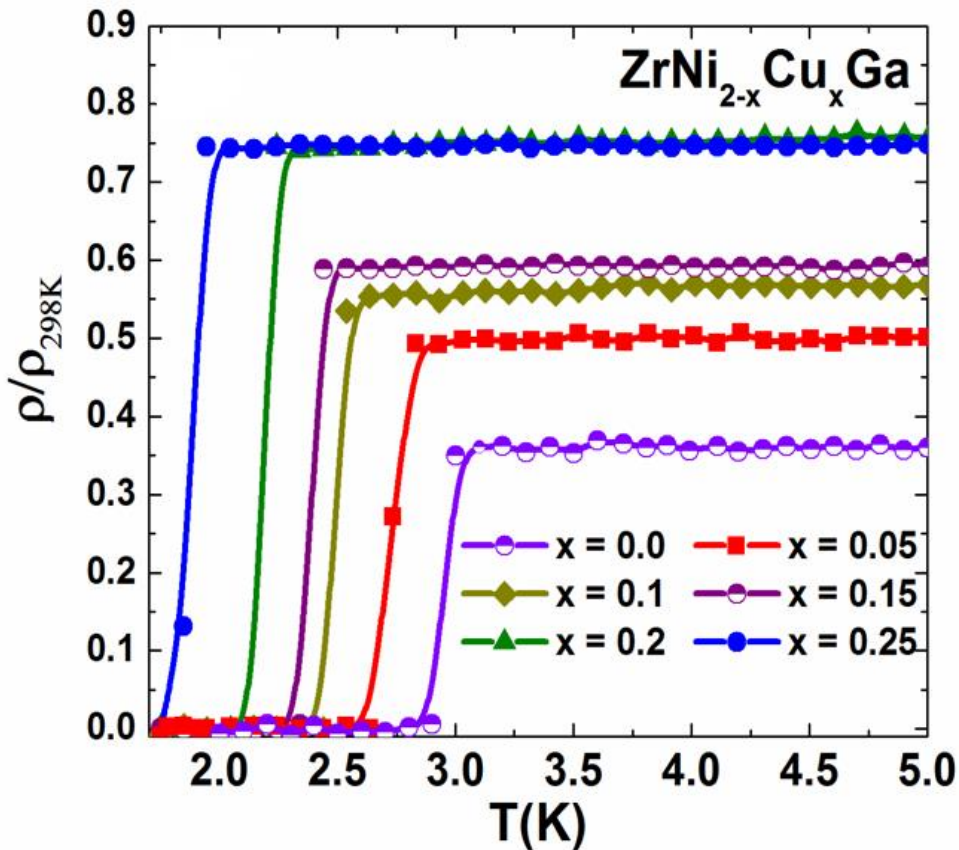


Figure 4.9 Temperature dependence of the resistivity for $\text{ZrNi}_{2-x}\text{Cu}_x\text{Ga}$

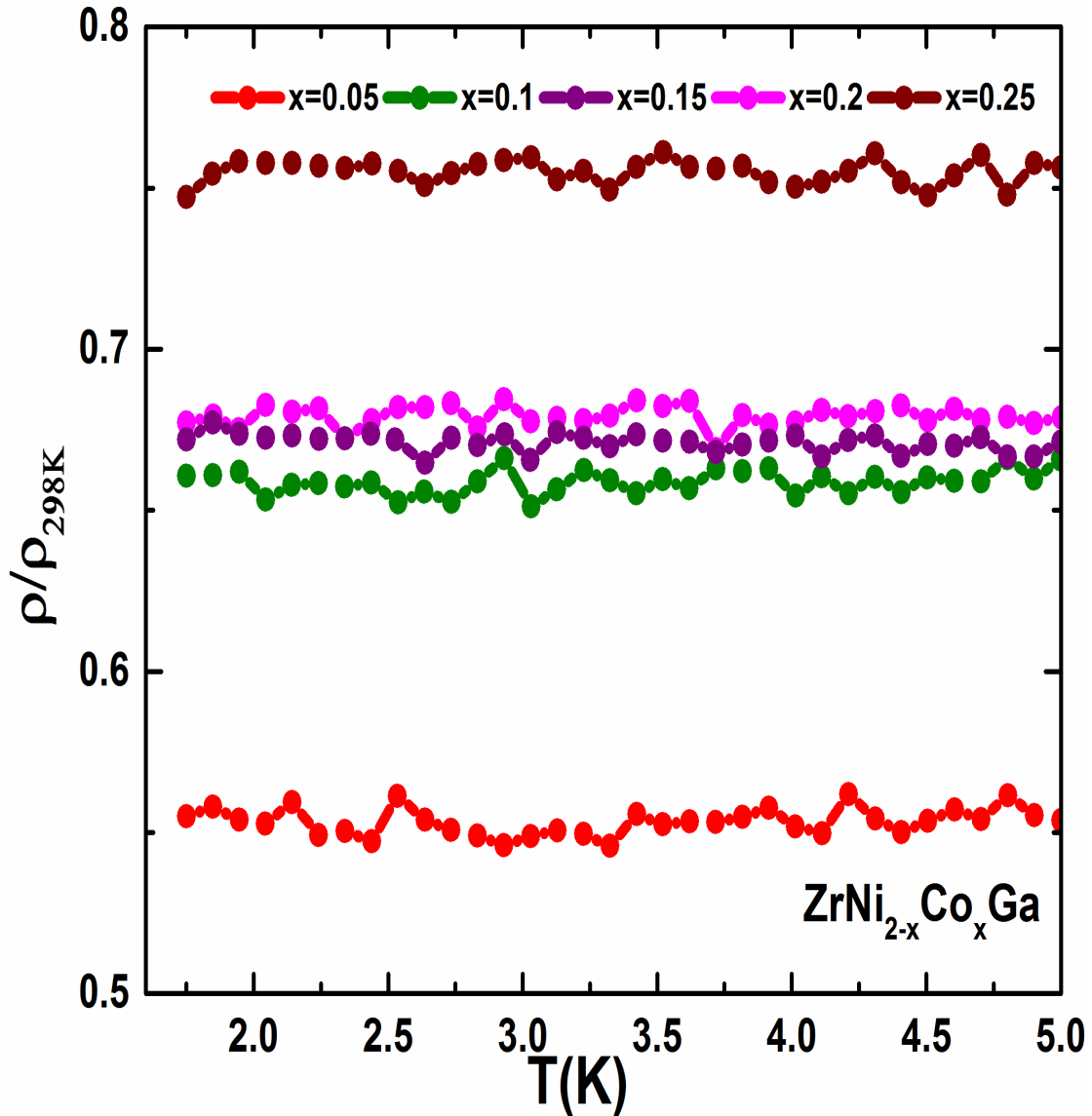


Figure 4.10 Temperature dependence of the resistivity for $\text{ZrNi}_{2-x}\text{Co}_x\text{Ga}$

Figure 4.11 shows the $\rho(T)$ measurement data for $\text{ZrNi}_2\text{Ga}_{1-x}\text{Al}_x$ compounds. All of the compounds showed superconducting behavior at low temperature as expected. Before the superconducting transition, a sharp drop in resistivity was also observed, which is vivid for the $x = 0.25$ compound. The resistivity drop occurred at 9 K for $x = 0.25$ and was observed in other compounds as well. The superconducting transition temperature for $x=0.25$ compounds was recorded to be 2.7 K which went on decreasing for increasing x . More importantly, it was found that the T_c for $x = 1$, (ZrNi_2Al), was found to be 2.2 K which is larger than the earlier reported value of 1.38K⁶⁹. The unusual

resistivity behavior observed above the superconducting transition needs further investigation. Due to lack of time, further experiments couldn't be carried out to study this phenomenon.

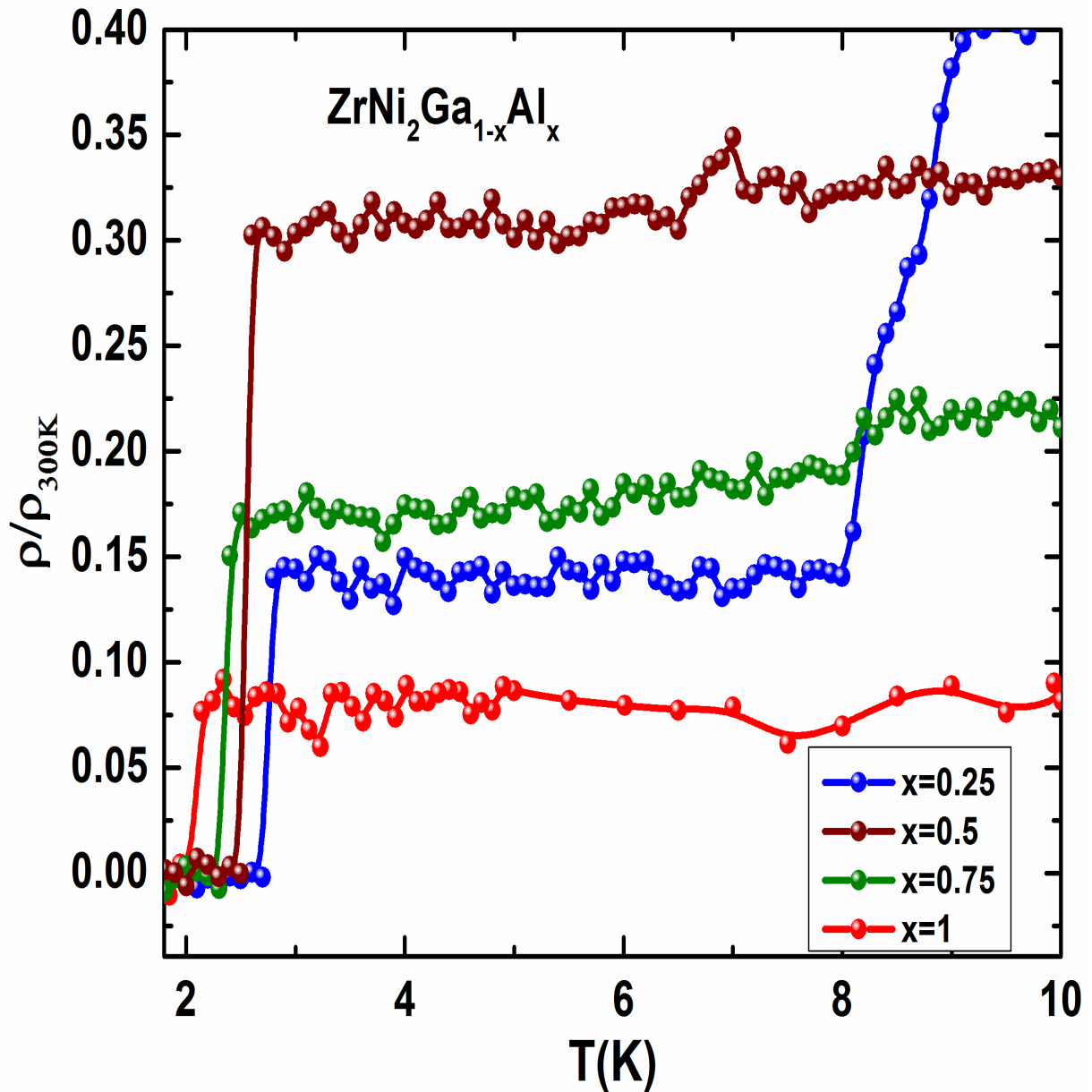


Figure 4.11 Temperature dependent resistivity of $\text{ZrNi}_2\text{Ga}_{1-x}\text{Al}_x$

4.2.2 Resistivity versus Magnetic field, $\rho(H)$

The resistivity as a function of applied magnetic field is as shown in Figure 4.12. The upper critical field, H_{c2} , decreases with the increasing concentration of Cu in $ZrNi_{2-x}Cu_xGa$ with the values ranging from ~ 0.15 T (for $x=0.25$) to ~ 0.75 T (for $x=0.05$). This significantly decreasing value of upper critical field reflects the weakening of superconductivity as the Cu concentration increases. The resistivity data were measured at 2 K temperature. The $\rho(H)$ data for Co-doped compounds didn't show such field transitions.

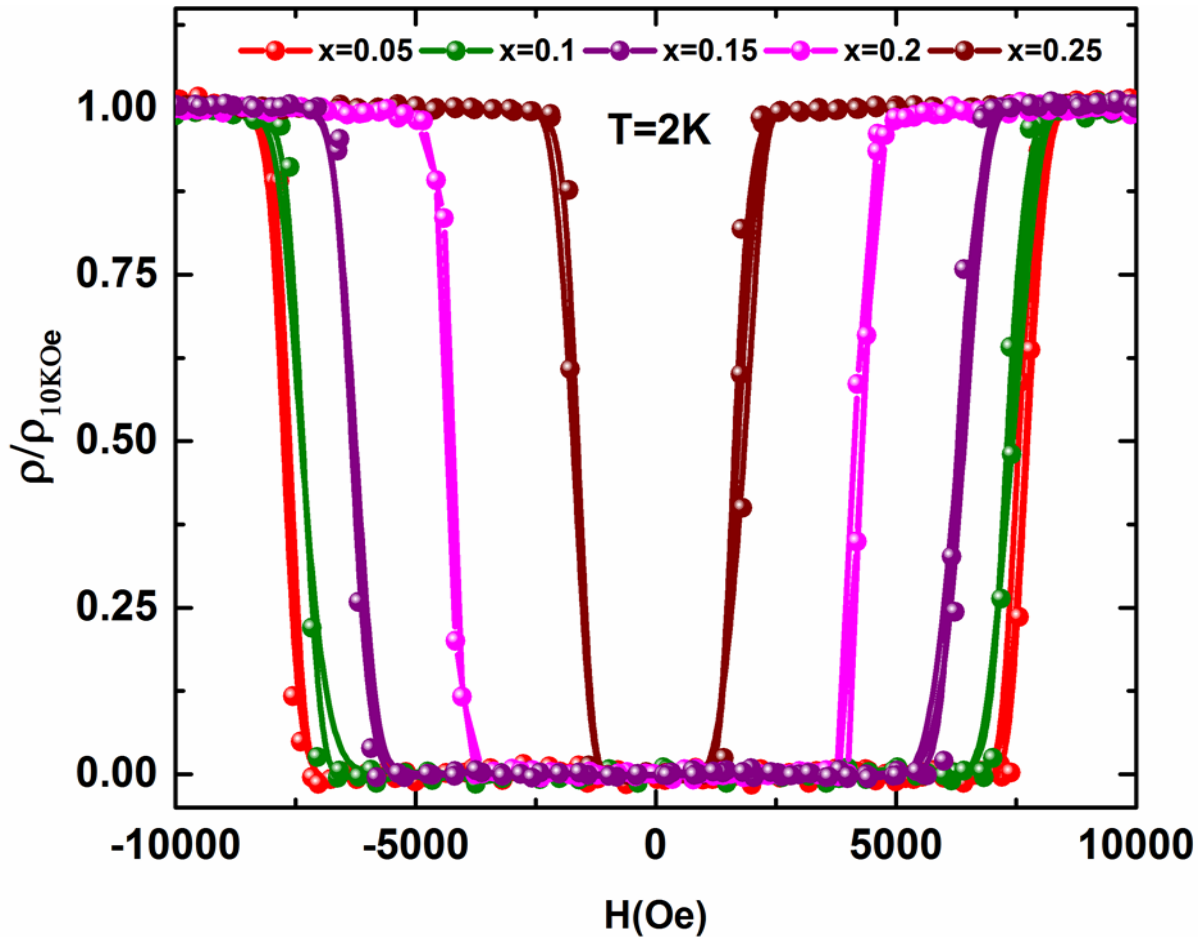


Figure 4.12 Normalized resistivity versus magnetic field for $ZrNi_{2-x}Cu_xGa$

4.3 Magnetization measurements

The magnetization measurements were performed in both the $ZrNi_{2-x}Cu_xGa$ and $ZrNi_{2-x}Co_xGa$ compounds using the vibrating sample magnetometer option on the PPMS. The dc magnetization

versus temperature, $M(T)$, measurements were performed at a constant magnetic field of 25 Oe which is small enough not to destroy the superconductivity. The magnetization versus applied magnetic field, $M(H)$, data were collected at a 2 K temperature. The ac susceptibility versus temperature measurement was performed using the ACMS option at a temperature range of 2 K to 10 K in an ac field of 10 Oe with applied frequencies of 10 Hz, 100 Hz, 1 kHz.

4.3.1 Magnetization versus Temperature, $M(T)$

The Magnetization data as a function of temperature is shown here for only those series which showed superconductivity. The $ZrNi_{2-x}Cu_xGa$ and $ZrNi_2Ga_{1-x}Al_x$ compounds showed superconducting transition in $M(T)$ graph while $ZrNi_{2-x}Co_xGa$ compounds did not.

Figure 4.13 shows the $M(T)$ data for $ZrNi_{2-x}Cu_xGa$ compounds measured in a static magnetic field of 25 Oe. The superconducting compounds are characterized by a negative magnetization below T_C and zero magnetization above T_C . It should be noted that no SC transition is observed in the $M(T)$ data for the sample with $x = 0.25$. This is because the SC transition for this alloy occurs below 2 K as shown in the $\rho(T)$ data (as in Figure 4.10), while the minimum temperature during $M(T)$ data collection was 2 K. The transition temperatures for the rest of the Cu doped alloys are consistent with the temperature obtained from the $\rho(T)$ data. The T_C 's of the $ZrNi_{2-x}Cu_xGa$ compounds as a function of Cu concentration x are plotted in the inset of Figure 4.13. As shown in the figure, T_C linearly decreases with increasing Cu concentration from 2.97 K ($x = 0.0$) to 1.85 K ($x = 0.25$). Although no samples with $x > 0.25$ were investigated, a linear extrapolation of the T_C vs. x data suggests that superconductivity in $ZrNi_{2-x}Cu_xGa$ may disappear for $x > 0.6$. No superconductivity was observed in the $M(T)$ data for the $ZrNi_{2-x}Co_xGa$ compounds (not shown here), which is consistent with the $\rho(T)$ data for the compounds.

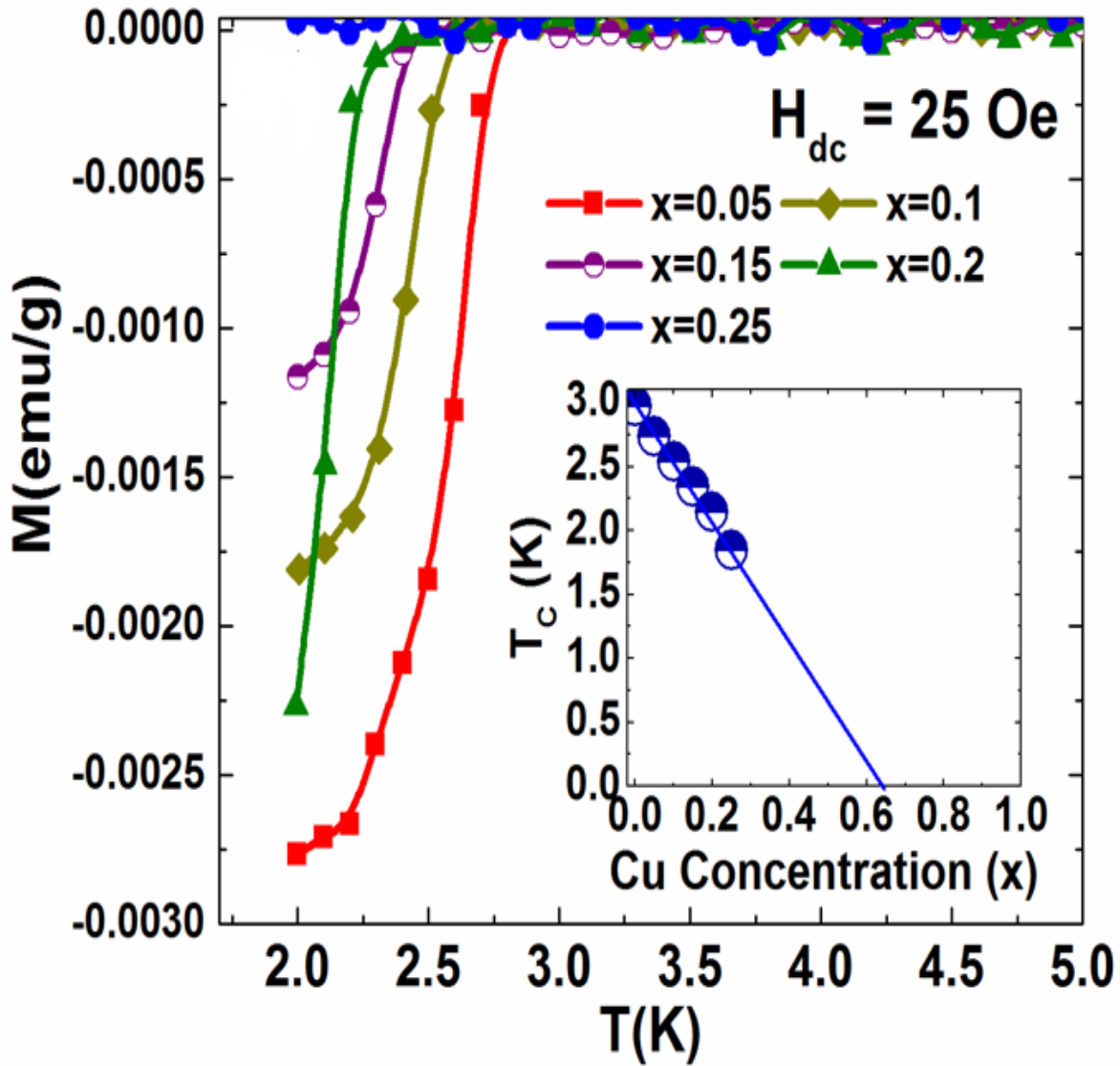


Figure 4.13 The dc magnetization of $ZrNi_{2-x}Cu_xGa$. The inset shows T_c as a function of Cu concentration x .

The $M(T)$ data for $ZrNi_2Ga_{1-x}Al_x$ compounds are as shown in Figure 4.14 (for $x = 0.5, 0.75, 0.1$) and Figure 4.15 (for $x = 0.25$). All the compounds show zero magnetization until a temperature in the vicinity of 9 K. An unusual behavior is observed suggesting a new phase transition before the superconducting transition which eventually occurs between 2.2 K to 2.7 K. The superconducting transition for all the samples is consistent with the T_c observed in resistivity measurement. The continuous drop in magnetization at 9 K shows the behavior of second order phase transition which

might be the case for these compounds. This behavior is consistent with the resistivity drop for each of the compounds in this series at the same temperature where the resistivity can be seen to fall significantly for $x=0.25$ and a visible slope in $\rho(T)$ data for all compounds.

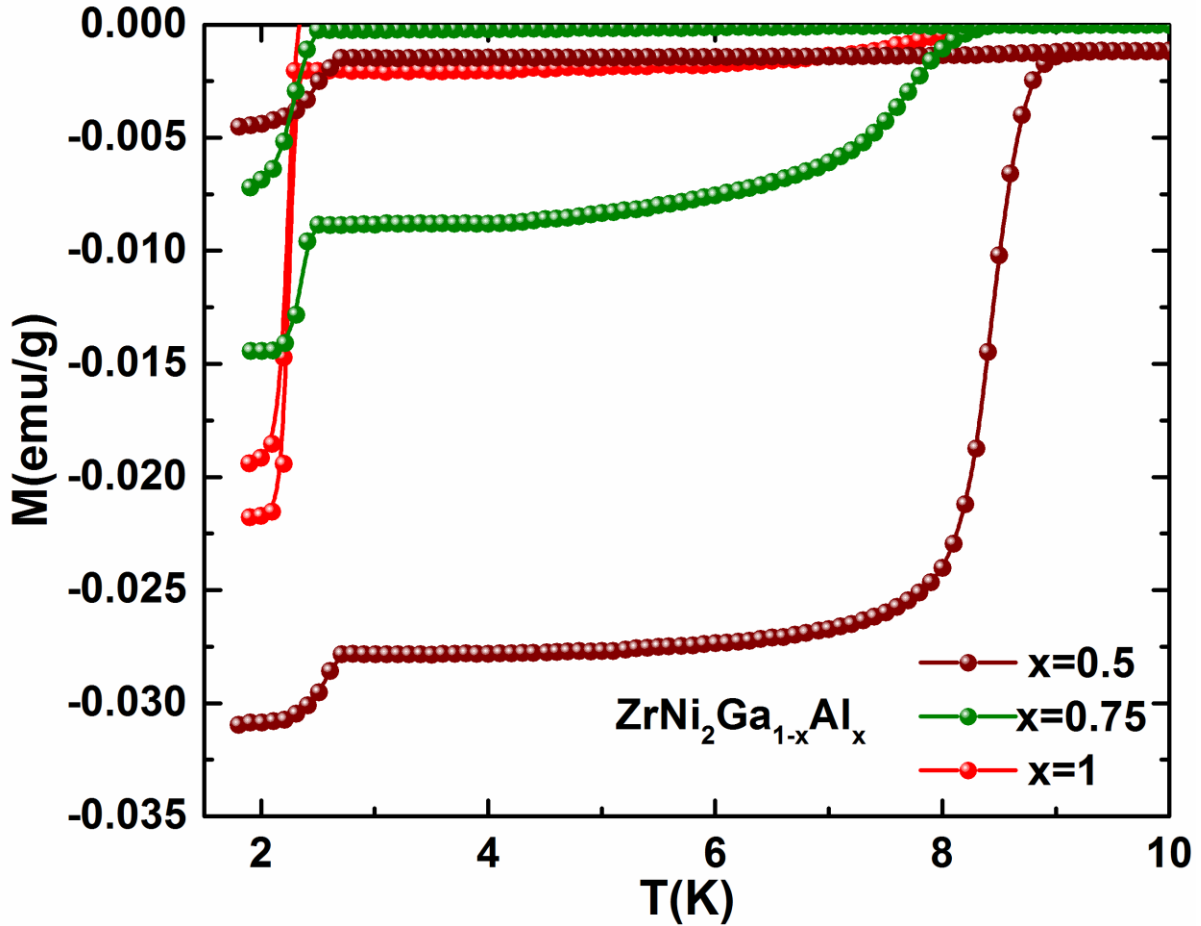


Figure 4.14 The dc magnetization of $\text{ZrNi}_2\text{Ga}_{1-x}\text{Al}_x$ compounds

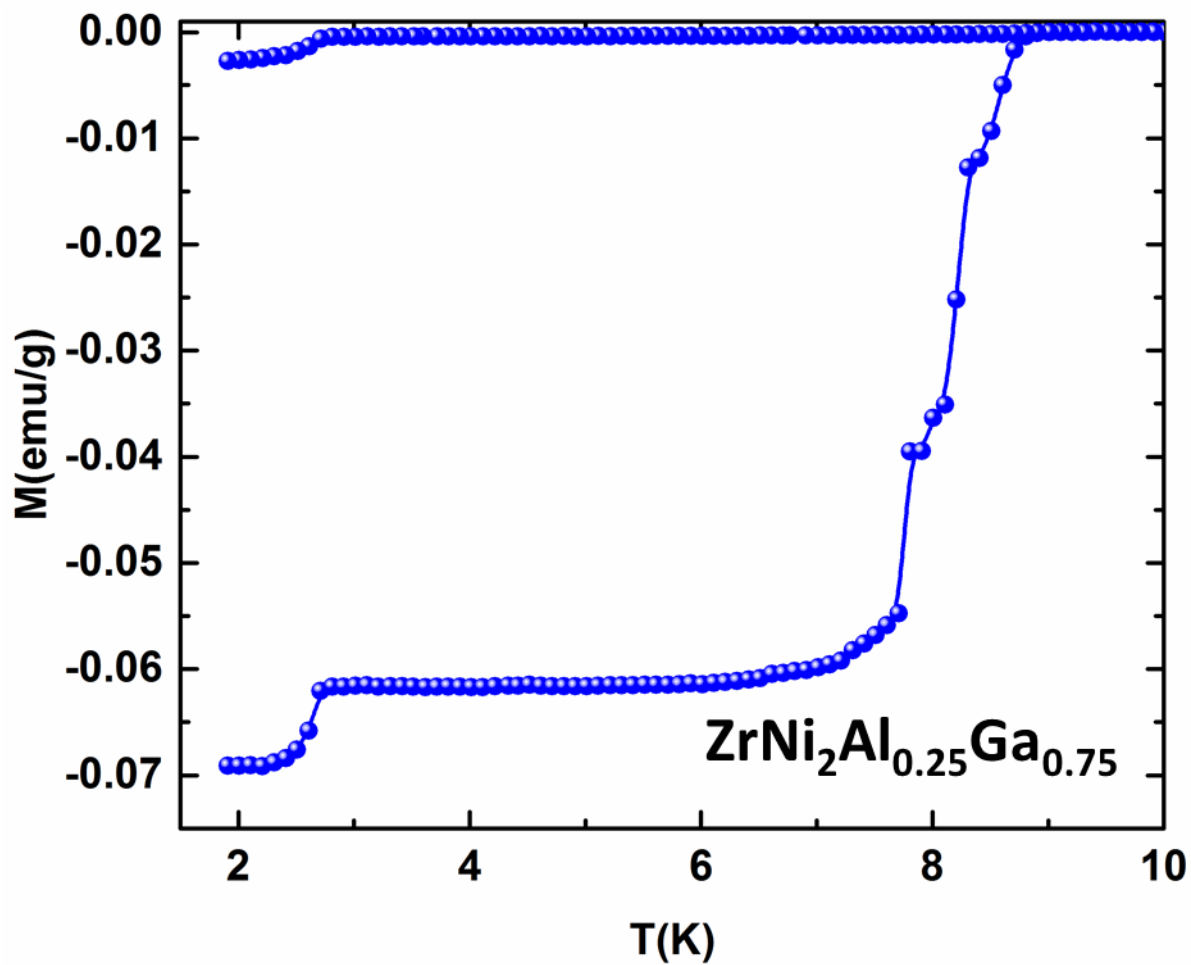


Figure 4.15 The dc magnetization of $\text{ZrNi}_2\text{Al}_{0.25}\text{Ga}_{0.75}$

4.3.2 Magnetization versus Magnetic Field, $M(H)$

The $M(H)$ data for the $ZrNi_{2-x}Cu_xGa$ and $ZrNi_{2-x}Co_xGa$ compounds, measured under ZFC condition at $T = 2$ K, are shown in Figure 4.16 and Figure 4.17 respectively. All the Cu doped alloys with $x < 0.25$ exhibit the butterfly loop typical for type II BCS superconductors. Although all the Cu doped samples with $x < 0.25$ exhibit the butterfly loop at 2 K, the amplitude of the loops diminishes with increasing Cu concentration and completely disappears for $x = 0.25$. As shown in the inset of Figure 4.16, the alloy with $x = 0.25$ exhibits a typical paramagnetic behavior. The $M(H)$ data for the $ZrNi_{2-x}Co_xGa$ compounds, as shown in Figure 4.17, demonstrate that all the Co-doped compounds exhibit paramagnetic behavior, and the behavior is enhanced with increasing Co concentration. Additionally, a small hysteresis is observed in the low field region of the $M(H)$ data for the Co-doped sample with $x = 0.25$, which indicates the presence of ferromagnetic interactions in the compound. The presence of Co-rich regions in the sample (as shown in the SEM images in Figure 4.7) may be responsible for this behavior. However, more measurements are necessary to confirm this argument.

Figure 4.18 shows the field dependent magnetization of $ZrNi_2Ga_{1-x}Al_x$ compounds measured at 2 K. All the compounds exhibit the typical butterfly loop but in diminishing order of amplitude as the Al concentration increases. The loop exhibits an irregularity in magnetization which is not seen in the parent compound $ZrNi_2Ga$. The magnetization decreases initially as the field increases until at one point ($H=2000$ Oe for $x=0.25$ and $H\sim 2500$ Oe for $x=0.5$) where the magnetization becomes flat and again decreases exponentially. Since the XRD data and SEM imaging do not show any significant structural and compositional variations, this behavior couldn't be explained and needs further investigation.

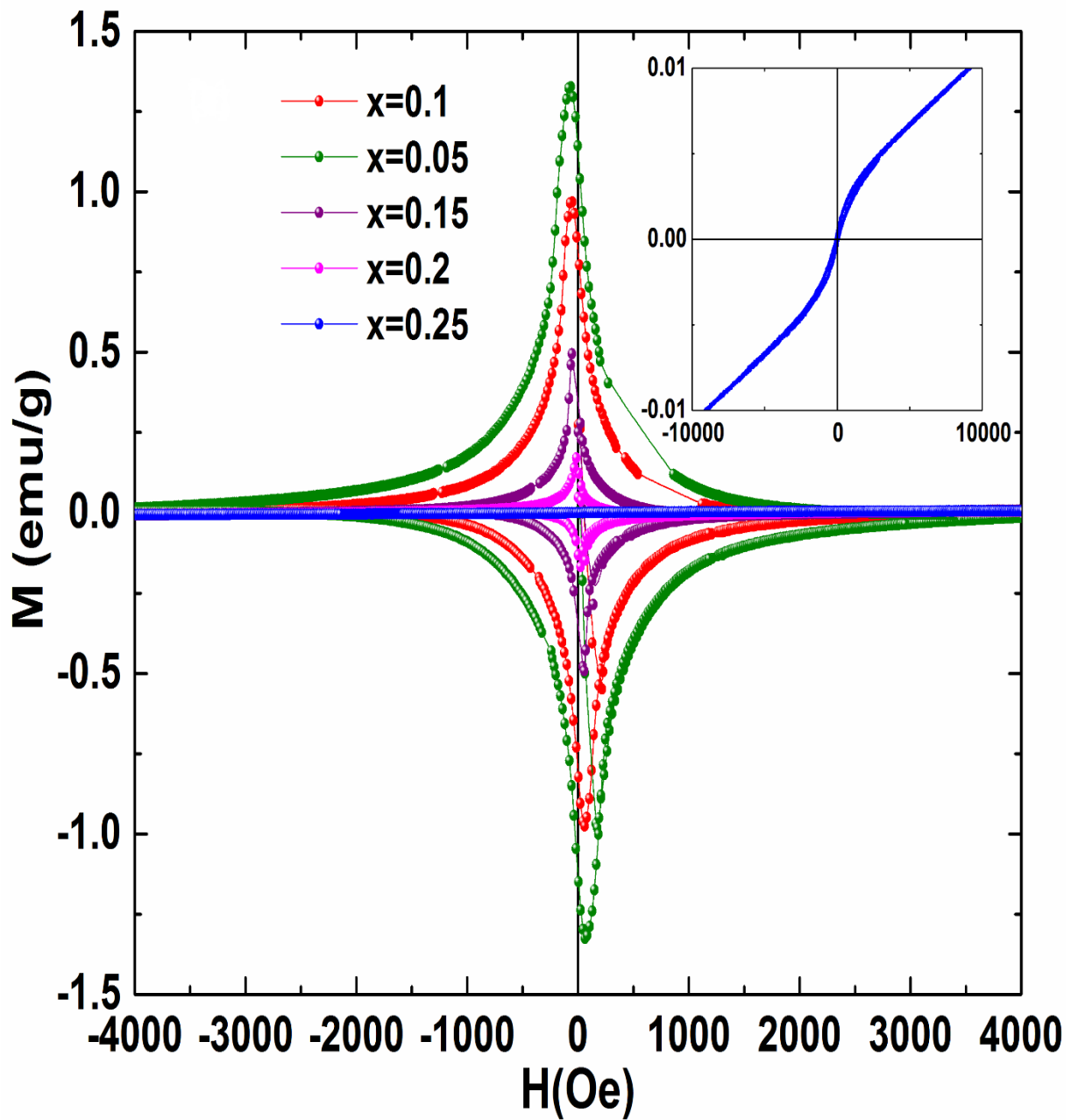


Figure 4.16 Field dependence of the magnetization of $ZrNi_{2-x}Cu_xGa$ measured at 2 K.

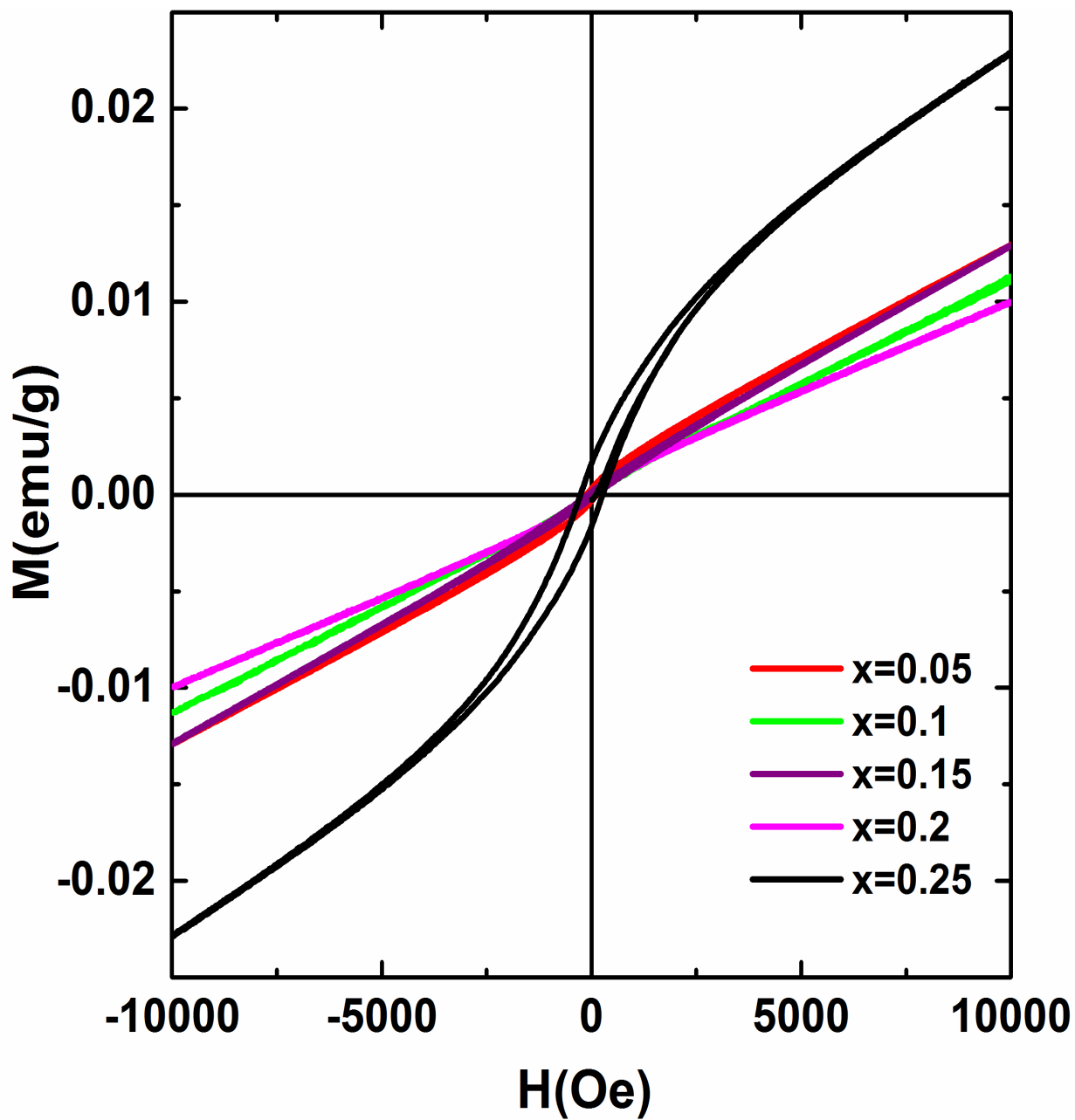


Figure 4.17 Field dependence of the magnetization of $ZrNi_{2-x}Co_xGa$ measured at 2 K.

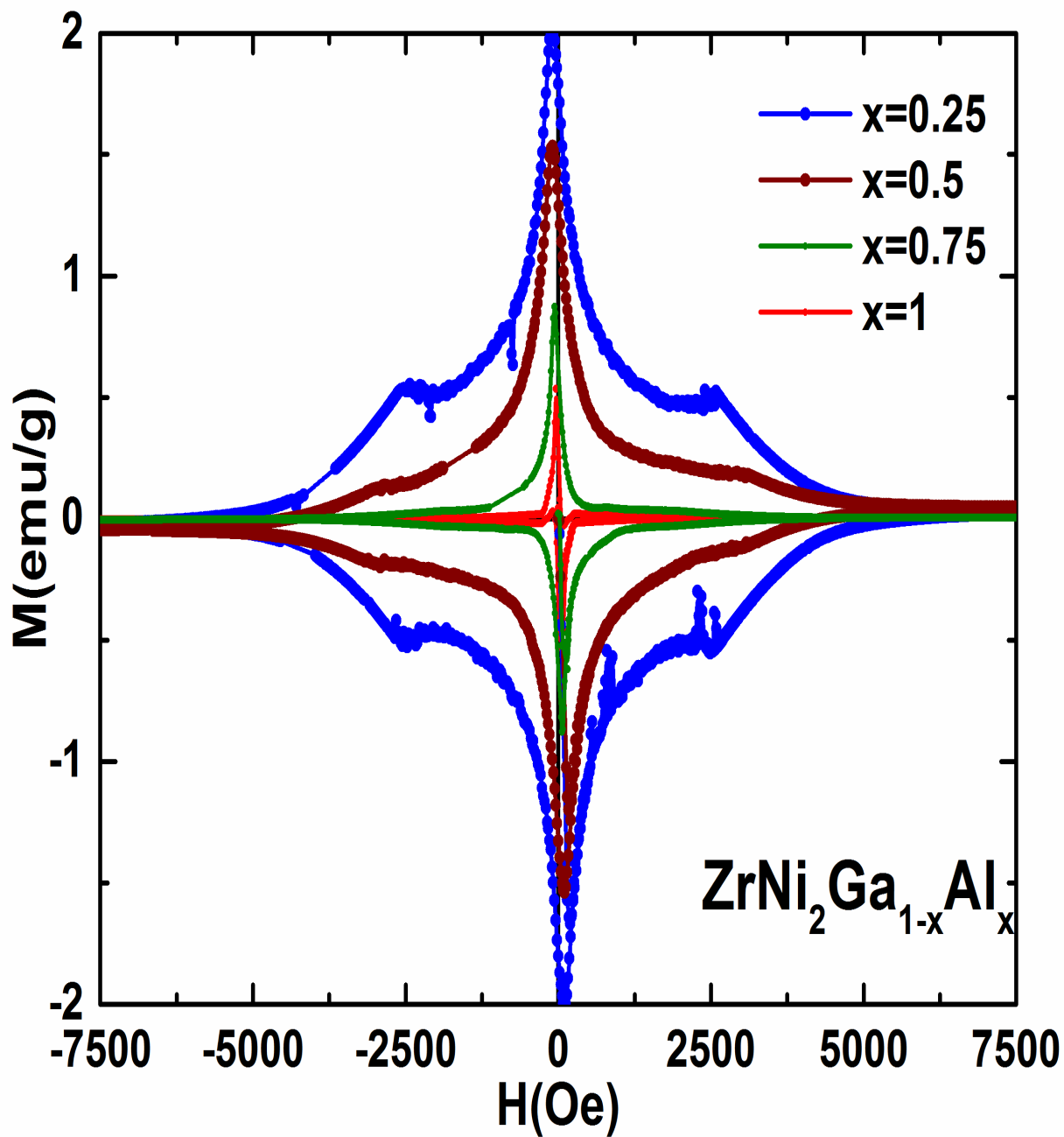


Figure 4.18 Field dependence of the magnetization of $\text{ZrNi}_2\text{Ga}_{1-x}\text{Al}_x$ measured at 2 K.

4.3.3 AC Susceptibility versus temperature

The temperature dependence of the real component of the ac magnetic susceptibility $\chi'(T)$ for selected $\text{ZrNi}_{2-x}\text{Cu}_x\text{Ga}$ materials are shown in Figure 4.19. SC transitions, signified by a sharp drop in χ' below T_C , are observed for all samples. Earlier it was shown that due to flux creeping, the sample with $x = 0$ (ZrNi_2Ga) exhibits a noticeable frequency dependence, where T_C shifts to lower temperature with increasing frequency. As shown in Figure 4.19, no such frequency dependence is observed in the Cu doped alloys, suggesting a weakening of SC interactions in the $\text{ZrNi}_{2-x}\text{Cu}_x\text{Ga}$ compounds.

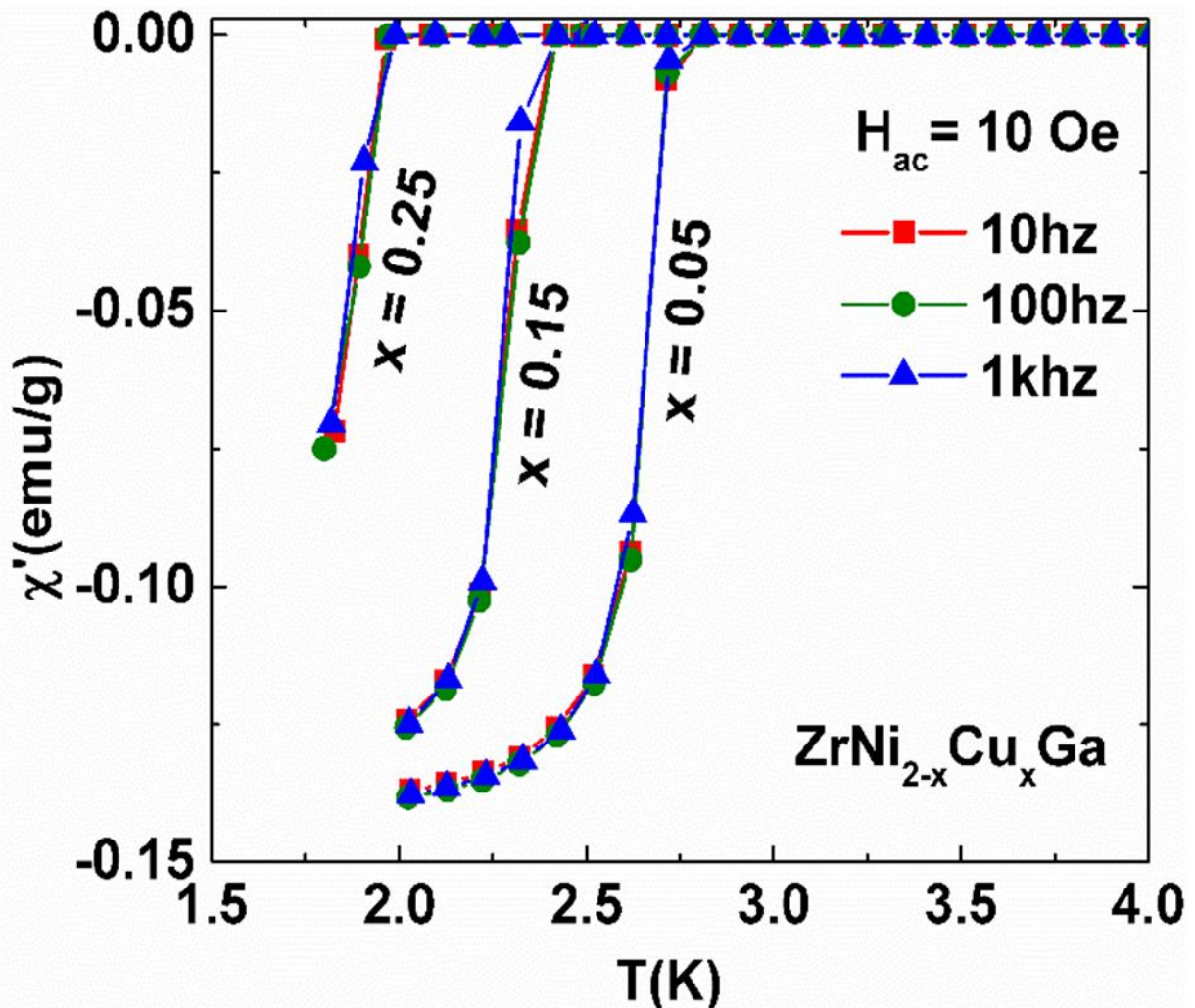


Figure 4.19 Real components of the ac susceptibility of selected $\text{ZrNi}_{2-x}\text{Cu}_x\text{Ga}$ compounds.

Figure 4.20 shows the ac susceptibility measurement data for the $\text{ZrNi}_2\text{Ga}_{1-x}\text{Al}_x$ compounds. The real component of ac susceptibility shows a vague frequency dependence on superconducting transition temperature. The transition that was observed in $M(T)$ data and $\rho(T)$ data was further boosted by the ac susceptibility data where a clear transition can be seen for each compound although the frequency dependence was not seen for this transition as well.

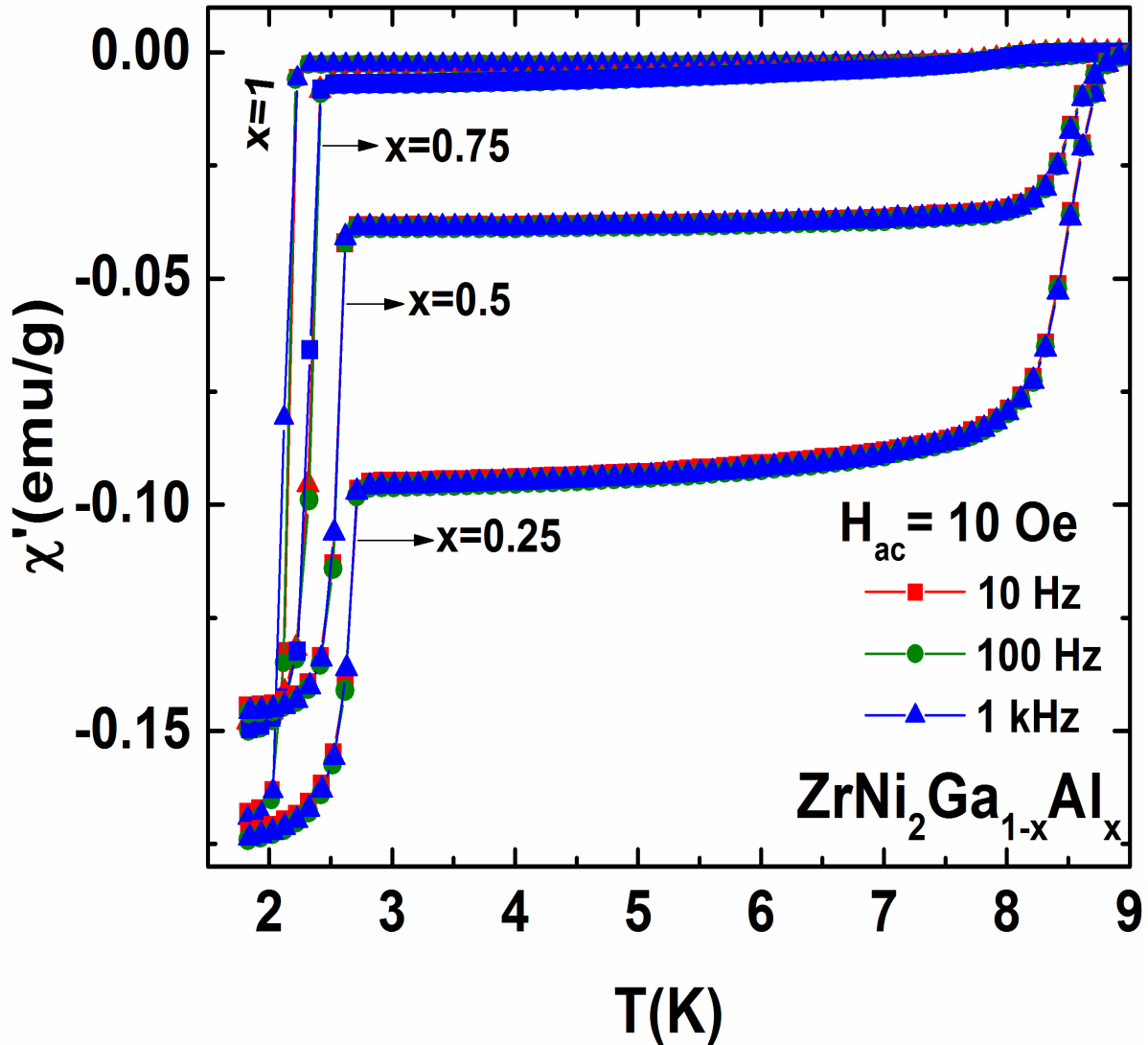


Figure 4.20 Real components of the ac susceptibility of selected $\text{ZrNi}_2\text{Ga}_{1-x}\text{Al}_x$ compounds.

Chapter 5: Conclusion

In a nutshell, the superconducting properties of $\text{ZrNi}_{2-x}\text{Cu}_x\text{Ga}$, $\text{ZrNi}_{2-x}\text{Co}_x\text{Ga}$ and $\text{ZrNi}_2\text{Ga}_{1-x}\text{Al}_x$ compounds have been investigated in detail. The crystal structure of all the three series of compounds were found to be in agreement with the parent Heusler compound ZrNi_2Ga . All the doped compounds showed $L2_1$ cubic structure with some minor variations in intensities of some characteristic peaks. The insertion of doped atoms did not change the ordering of lattice significantly thereby keeping the same crystal structure. The lattice parameters were found to be changed from that of parent compound in accordance with the size of atomic radii of the dopants as predicted. With the increase of Cu concentration, the superconducting properties gradually vanished, and the paramagnetic ordering was enhanced while a small amount of Co as low as $x=0.05$ in the $\text{ZrNi}_{2-x}\text{Co}_x\text{Ga}$ series changed the whole properties of parent compound showing paramagnetic behavior in all the compounds except for $x = 0.25$ which showed a magnetic hysteresis suggesting a ferromagnetic ordering of the sample. All the Al-doped compounds showed superconducting properties, but it was found to be gradually weakened as the doping was increased. The SEM imaging and EDS analysis provided additional light on the compositions showing a near homogeneity for all the samples.

The resistivity data showed the temperature dependent resistivity for all the samples. All the Cu-doped compounds showed a sharp drop in resistivity to zero at different temperatures below 2.7 K in a decreasing order with increased Cu concentration. The critical magnetic fields also revealed the weakening of superconductivity with the decrement in its values with increasing Cu concentration while such resistivity drop, and magnetic behavior were not observed in Co-doped compounds. All the Al-doped compounds showed zero resistivity below the T_c of parent compound. The open-air annealing effect was observed in resistivity data of $\text{ZrNi}_2\text{Ga}_{1-x}\text{Al}_x$ compounds showing a significant drop in resistivity before the superconducting transition.

The magnetization measurements confirmed the weakening of superconductivity in $\text{ZrNi}_{2-x}\text{Cu}_x\text{Ga}$ and a complete vanishing of superconductivity in $\text{ZrNi}_{2-x}\text{Co}_x\text{Ga}$. M-T measurement showed no phase transition in $\text{ZrNi}_{2-x}\text{Co}_x\text{Ga}$, while the phase transition for $\text{ZrNi}_{2-x}\text{Cu}_x\text{Ga}$ occurred is consistent with the temperature determined by resistivity measurement. A double phase transition

was observed in $\text{ZrNi}_2\text{Ga}_{1-x}\text{Al}_x$ compounds; the first transition remaining unknown and the second being the superconducting one. The M-H measurements for $\text{ZrNi}_{2-x}\text{Cu}_x\text{Ga}$ and $\text{ZrNi}_2\text{Ga}_{1-x}\text{Al}_x$ showed the butterfly loop typical for a Type-II superconductor with diminishing loop amplitude for increasing dopant concentration showing the weakening of superconductivity and strengthening of paramagnetic ordering whereas all the $\text{ZrNi}_{2-x}\text{Co}_x\text{Ga}$ compounds showed a complete paramagnetic behavior for $x < 0.2$ and ferromagnetic ordering for $x = 0.25$.

From the ACMS measurements, it was found that the T_c of $\text{ZrNi}_{2-x}\text{Cu}_x\text{Ga}$ compounds did not show a sharp dependence on the frequencies in an applied range of 10 Hz to 1000 Hz. The same result was observed for $\text{ZrNi}_2\text{Ga}_{1-x}\text{Al}_x$ compounds. Overall, all the measurement data showed that the doping of non-magnetic elements Cu and Al weakened, and a magnetic element Co destroyed the superconductivity of Heusler compound ZrNi_2Ga .

References

- ¹ Onnes, H. Kamerlingh. "The resistance of pure mercury at helium temperatures." *Commun. Phys. Lab. Univ. Leiden* 12.120 (1911): 1.
- ² Keeley, T. C., K. Mendelssohn, and J. R. Moore. "Experiments on superconductors." *Nature* 134.3394 (1934): 773-774.
- ³ Hajenius, M., et al. "Low noise NbN superconducting hot electron bolometer mixers at 1.9 and 2.5 THz." *Superconductor Science and Technology* 17.5 (2004): S224.
- ⁴ Wu, Maw-Kuen, et al. "Superconductivity at 93 K in a new mixed-phase Y-Ba-Cu-O compound system at ambient pressure." *Physical Review Letters* 58.9 (1987): 908.
- ⁵ Drozdov, A. P., et al. "Conventional superconductivity at 203 kelvin at high pressures in the sulfur hydride system." *Nature* 525.7567 (2015): 73-76.
- ⁶ Bardeen, John, Leon N. Cooper, and John Robert Schrieffer. "Theory of superconductivity." *Physical Review* 108.5 (1957): 1175.
- ⁷ Meissner, Walther, and Robert Ochsenfeld. "Ein neuer effekt bei eintritt der supraleitfähigkeit." *Naturwissenschaften* 21.44 (1933): 787-788.
- ⁸ Landau, Lev Davidovich, and V. L. Ginzburg. "On the theory of superconductivity." *Zh. Eksp. Teor. Fiz.* 20 (1950): 1064.
- ⁹ Poole, Charles K., Horacio A. Farach, and Richard J. Creswick. *Handbook of superconductivity*. Academic Press, 1999.
- ¹⁰ M. Ishikawa, J. L. Jorda, and A. Junod, *Superconductivity in d and f-Band Metals 1982*, edited by W. Buckel and W. Weber (Kernforschungszentrum Karlsruhe, Germany, 1982).
- ¹¹ J. Winterlik, G. H. Fecher, C. Felser, M. Jourdan, K. Grube, F. Hardy, H. von Löhneysen, K. L. Holman, and R. J. Cava, *Phys. Rev. B* 78, 184506 (2008).
- ¹² T. Klimczuk, C. H. Wang, K. Gofryk, F. Ronning, J. Winterlik, G. H. Fecher, J.-C. Griveau, E. Colineau, C. Felser, J. D. Thompson, D. J. Safarik, and R. J. Cava, *Phys. Rev. B* **85**, 174505 (2012).
- ¹³ L. van Hove, *Phys. Rev.* 89, 1189 (1953).
- ¹⁴ Saad Alzahrani, Mahmud Khan, *AIP Advances*, **7**, 055706 (2017)

-
- ¹⁵ De Haas, W. J., J. De Boer, and G. J. Van den Berg. "The electrical resistance of gold, copper and lead at low temperatures." *Physica* 1.7-12 (1934): 1115-1124
- ¹⁶ Jackson, L. C., and H. Preston-Thomas. "Superconductivity of niobium." *The London, Edinburgh, and Dublin Philosophical Magazine and Journal of Science* 41.323 (1950): 1284-1287.
- ¹⁷ Wexler, Aaron, and W. S. Corak. "Superconductivity of Vanadium." *Physical Review* 79.4 (1950): 737.
- ¹⁸ Ziegler, W. T. "The Superconductivity of Lanthanum and Cerium1." *The Journal of Chemical Physics* 16.8 (1948): 838-839.
- ¹⁹ Burton, E. F. "Supraconductivity of films of tin." *Nature* 133 (1934): 459
- ²⁰ Boato G., Gallinaro G., Rizzuto C. "Effect of transition metal impurities on the critical temperature of superconducting Al, Zn, In, and Sn. *Physical Review*, 1966 – APS.
- ²¹ Meissner, Walther, and Robert Ochsenfeld. "Ein neuer effekt bei eintritt der supraleitfähigkeit." *Naturwissenschaften* 21.44 (1933): 787-788.
- ²² London, F. & London, H. *The Electromagnetic Equations of the Supraconductor*. Proc. R. Soc. Lond. A 149, 71–88 (1935).
- ²³ <https://upload.wikimedia.org/wikipedia/commons/b/b5/EfektMeisnera.svg>
- ²⁴ Hill, E. L. "Superconductivity in Metals." *Review of Scientific Instruments* 4.1 (1933): 3-6.
- ²⁵ Rjabinin, J. N., and L. W. Shubnikow. "Magnetic properties and critical currents of superconducting alloys." *Nature* 135.3415 (1935): 581-582.
- ²⁶ G.Achermann, E. Friderich, E. Justi and J. Kramer: *Z. Phys.* 42 (1941) 349.
- ²⁷ Matthias, B. T., et al. "Superconductivity of Nb₃Sn." *Physical Review* 95.6 (1954): 1435.
- ²⁸ T.G. Berlincourt and R.R. Hake (1962). "Pulsed-Magnetic-Field Studies of Superconducting Transition Metal Alloys at High and Low Current Densities". *Bulletin of the American Physical Society*. II-7: 408.
- ²⁹ Bednorz, J. G.; Müller, K. A. (1986). "Possible high T_C superconductivity in the Ba-La-Cu-O system". *Zeitschrift für Physik B*. 64 (2): 189–193.
- ³⁰ Francois, M., et al. "Structural phase transition at 150K in the high-temperature superconductor La_{1.85}Sr_{0.15}CuO₄." *Solid state communications* 63.1 (1987): 35-40.
- ³¹ Hazen, R. M., et al. "100-K superconducting phases in the Tl-Ca-Ba-Cu-O system." *Physical Review Letters* 60.16 (1988): 1657.

-
- ³² Kamihara, Y; Watanabe, T; Hirano, M; Hosono, H. "Iron-Based Layered Superconductor La[O_{1-x}F_x]FeAs (x=0.05–0.12) with $T_c = 26$ K". *Journal of the American Chemical Society*. 130.11 (2008): 3296–3297
- ³³ Wang, Qing-Yan; Li, Zhi; Zhang, Wen-Hao; Zhang, Zuo-Cheng; Zhang, Jin-Song; Li, Wei; Ding, Hao; Ou, Yun-Bo; Deng, Peng; Chang, Kai; Wen, Jing; Song, Can-Li; He, Ke; Jia, Jin-Feng; Ji, Shuai-Hua; Wang, Ya-Yu; Wang, Li-Li; Chen, Xi; Ma, Xu-Cun; Xue, Qi-Kun. "Interface-Induced High-Temperature Superconductivity in Single Unit-Cell FeSe Films on SrTiO₃". *Chin. Phys. Lett.* 29.3 (2012): 037402.
- ³⁴ Drozdov, A. P., et al. "Conventional superconductivity at 203 kelvin at high pressures in the sulfur hydride system." *Nature* 525.7567 (2015): 73-76.
- ³⁵ Li Y., Hao, J., Li, Y. & Ma, Y. The metallization and superconductivity of dense hydrogen sulfide. *J. Chem. Phys.* 140, 174712 (2014)
- ³⁶ James F. Annett. *Superconductivity, Superfluids and Condensates*. Oxford. (2004) p. 58.
- ³⁷ Tinkham, M. *Introduction to Superconductivity* (McGraw-Hill, New York, 1996), 2nd edn.
- ³⁸ Landau, Lev Davidovich, and V. L. Ginzburg. "On the theory of superconductivity." *Zh. Eksp. Teor. Fiz.* 20 (1950): 1064.
- ³⁹ Cohen L. F., Jensen H. J., "Open questions in magnetic behavior of high temperature superconductors" *Reports on Progress in Physics* 60.12 (1999): 1581
- ⁴⁰ <https://dc.edu.au/wp-content/uploads/cooper-pair-phonon.png>
- ⁴¹ Tinkham, M. *Introduction to Superconductivity* (McGraw-Hill, New York, 1996).
- ⁴² McMillan, W. L. "Transition temperature of strong-coupled superconductors." *Physical Review* 167.2 (1968): 331.
- ⁴³ Gottlieb U., Lasjaunias J. C., Tholence J. L., Laborde O., Thomas O., Madar R. "Superconductivity in TaSi₂ single crystals". *Phys. Rev. B.* 45.9 (1992): 4803–4806.
- ⁴⁴ Kriener, M; Muranaka, T; Kato, J; Ren, Z. A.; Akimitsu, J; Maeno, Y (2008). "Superconductivity in heavily boron-doped silicon carbide". *Sci. Technol. Adv. Mater.* 9.4 (2008): 044205.
- ⁴⁵ BB Goodman - *Reports on progress in physics*, 29 (1966): 445.
- ⁴⁶ Sidebottom, D. "Fundamentals of Condensed matter and Crystalline physics (Cambridge University Press, 2012).

-
- ⁴⁷ Schrieffer, J. R. & Brooks, J. S. "Handbook of high-temperature superconductivity: theory and experiment" (Springer, 2007).
- ⁴⁸ Norman, M. R. "Unconventional Superconductivity. In Novel Superfluids" (eds. Bennemann, K. H. & Ketterson, J. B.), vol. 2 (Oxford University Press, 2014).
- ⁴⁹ Monthoux, P.; Balatsky, A.; Pines, D. "Weak-coupling theory of high-temperature superconductivity in the antiferromagnetically correlated copper oxides". *Physical Review B*. 46. 22 (1992): 14803–14817.
- ⁵⁰ Heusler F. "Über magnetische Manganlegierungen". *Verhandlungen der Deutschen Physikalischen Gesellschaft* (in German). 12 (1903): 219.
- ⁵¹ Pierre J., Skolozdra R. V., Tobola J., Hordequin C., Kouacou M. A., Karla I., Currat R., and Lelievre-Berna E., *J. Alloys Compd.* 101 (1997): 262-263.
- ⁵² Schierning, Gabi, et al. "Concepts for medium-high to high temperature thermoelectric heat-to-electricity conversion: a review of selected materials and basic considerations of module design." *Translational Materials Research* 2.2 (2015): 025001.
- ⁵³ Kierstead H. A., Dunlap B.D., Malik S.K., Umarji A.M., and Shenoy G. K., *Phys. Rev. B* 32 (1985): 135.
- ⁵⁴ Wernick J. H., Hull G.W., Geballe T. H., Bernardini J.E., and Waszczak J.V., *Mater. Lett.* 2, 90 (1983).
- ⁵⁵ Seaman C. L., Dilley N. R., De Andrade M.C., Herrmann J., Maple M.B., and Fisk Z., *Phys. Rev. B* 53 (1996): 2651.
- ⁵⁶ Waki S., Yamaguchi Y., and Mitsugi K., *J. Phys. Soc. Jpn.* 54 (1985): 1673.
- ⁵⁷ Winterlik J., Fecher G. H., Thomas A., and Felser C., *Phys. Rev. B* 79 (2009): 064508.
- ⁵⁸ Kurtulus, Yasemin, et al. "Electronic structure and magnetic exchange coupling in ferromagnetic full Heusler alloys." *Physical Review B* 71.1 (2005): 014425.
- ⁵⁹ Webster P.J, Ziebeck K.R.A, *Journal of Physics and Chemistry of Solids*, 34.10 (1973): 1647-1654.
- ⁶⁰ Matthias B.T., *Phys. Rev.* 92 (1953): 874.
- ⁶¹ Matthias B.T., *Phys. Rev.* 97 (1955): 74.
- ⁶² Shelton R.N., Hausermann-Berg L.S., Johnson M.J., Klavins P., and Yang H.D, *Phys. Rev. B* 34 (1986): 199.

⁶³ <https://www.stresstech.com/en-fi/products/x-ray-diffraction-equipment/x-ray-diffraction/>

⁶⁴ <https://www.ssi.shimadzu.com/products/x-ray/onesight.html>

⁶⁵ http://www.bam.de/de/service/publikationen/powder_cell.htm

⁶⁶ <http://www.nanoimages.com/sem-technology-overview/>

⁶⁷ Corbari, L; et al. "Iron oxide deposits associated with the ectosymbiotic bacteria in the hydrothermal vent shrimp *Rimicaris exoculata*" *Biogeosciences*. 5.5 (2008): 1295–1310.

⁶⁸ PPMS Hardware Manual, 1070-150, Rev. B5, Quantum Design, Inc. (2008).

⁶⁹ Wernick J.H., Hull G.W., Geballe T.H., Bernardini J.E., and Waszczak J.B., *Mater. Lett.* 2, 90 (1983).